Harzburgite melting with and without H_2O: Experimental data and predictive modeling

Stephen W. Parman and Timothy L. Grove

Department of Earth, Atmosphere, and Planetary Sciences, Massachusetts Institute of Technology, Cambridge, Massachusetts, USA

Received 1 May 2003; revised 23 October 2003; accepted 30 October 2003; published 3 February 2004.

[1] The effect of H_2O on harzburgite-saturated melts has been quantified with a series of hydrous and anhydrous melting experiments using a piston-cylinder device. Experimental conditions were 1.2–2.2 GPa and 1175–1500°C. Melt H_2O contents range from 0 to 10 wt %. The effects of temperature, pressure, and bulk composition (including H_2O) on the SiO_2 content of the experimental melts have been evaluated using SiO_2 activity coefficients. The results suggest a two-lattice-type model for the melt phase in which H_2O mixes nearly ideally with other network modifiers (MgO, FeO, etc.) but does not mix on the network-forming lattice site and so has little effect on SiO_2 activity coefficients. The effect of H_2O on SiO_2 activity is too small to produce the high SiO_2 contents observed in mafic andesite magmas. It is proposed that the SiO_2-rich character of hydrous, subduction-related magmas is the result of the low temperatures at which hydrous melting occurs relative to anhydrous melting. Partition coefficients for MgO and FeO increase at lower temperatures, while the partition coefficient for SiO_2 is nearly constant and is buffered by olivine-orthopyroxene equilibria. Therefore the SiO_2/(MgO + FeO) ratios of harzburgite saturated melts increase as temperature falls in both hydrous and anhydrous systems. The results suggest that H_2O contents of andesitic magmas may be far higher (>7 wt %) than is generally accepted. Experimentally measured mineral/melt partition coefficients (this study and literature data) have been parameterized in terms of pressure, temperature, and melt H_2O content. These expressions have been used to construct a Gibbs-Duhem-based numerical model that predicts the compositions of hydrous and anhydrous olivine-orthopyroxene-saturated melts. Comparisons with experimental data not included in the model indicate that it is the most accurate model available for predicting the compositions of high-degree mantle melts, with or without H_2O. *INDEX TERMS:* 3630 Mineralogy and Petrology: Experimental mineralogy and petrology; 3640 Mineralogy and Petrology: Igneous petrology; 3655 Mineralogy and Petrology: Major element composition; *KEYWORDS:* mantle, melting, harzburgite, high-pressure, experimental, hydrous

Citation: Parman, S. W., and T. L. Grove (2004), Harzburgite melting with and without H_2O: Experimental data and predictive modeling, *J. Geophys. Res.*, *109*, B02201, doi:10.1029/2003JB002566.

1. Introduction

[2] At low extents of melting (<20%), melts of the Earth's upper mantle are in equilibrium with a lherzolite assemblage: olivine (ol), orthopyroxene (opx), clinopyroxene (cpx) and an aluminous phase (spinel, garnet, or plagioclase). The melts produced are basaltic in composition and are the most voluminous form of terrestrial mafic magmatism. The primary sites of basaltic volcanism are mid-ocean ridges (MOR) where melting occurs in the spinel stability field (1–3 GPa, Figure 1). As melting progresses, the first phase to be exhausted from the residue is cpx [e.g., *Baker and Stolper*, 1994]. Though spinel is still stable, it usually is <2% of the mass at the cpx-out point.

[3] As melting approaches the cpx-out boundary, melt production rates (dF/dT) rise, but once cpx is removed from the residue, melt production rates drop dramatically [*Asimow et al.*, 1997; *Hirschmann et al.*, 1999]. This effect may limit the upper bound of melting during adiabatic decompression at mid-ocean ridges [*Dick et al.*, 1984]. Plume-related magmas, thought to be produced by hot upwellings, also show little evidence for progressing past cpx-out, though one unusually mafic Hawaiian picrite has been shown to be in equilibrium with a harzburgite (ol + opx) residue [*Green et al.*, 2001; *Wagner and Grove*, 1998]. At present, mantle melting past cpx-out predominantly occurs when melting temperatures are lowered by hydrous fluids in subduction environments. This high-degree flux melting produces a spectrum of silica-rich melts: andesites, basaltic andesites and boninites (Figure 1). The high SiO_2 contents have typically been attributed to the effect of H_2O on the activities of various melt species [*Gaetani and*

0148-0227/04/2003JB002566$09.00

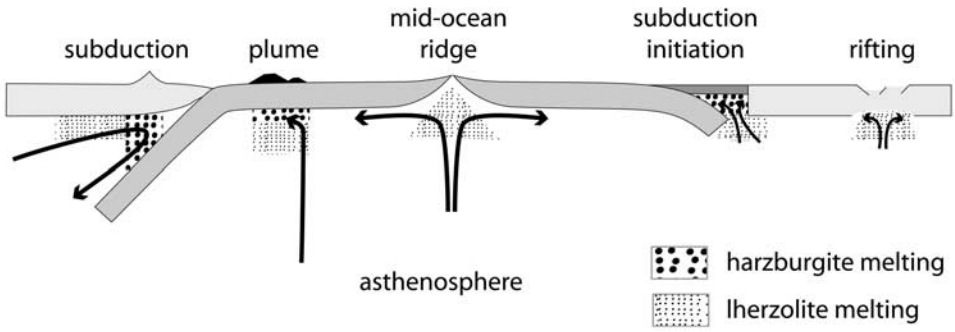

Figure 1. Tectonic settings where mantle melting proceeds past the cpx-out boundary. Lightly stippled areas indicate melting of ol + opx + cpx + sp (lherzolite). Heavily stippled areas indicate melting of ol + opx ± sp (harzburgite). Arrows indicate direction of mantle flow. In subduction zones, after an initial depletion event, hydrous melting often extends past cpx-out, producing magnesian andesites. Boninites record even higher degrees of melting, and are associated with transient processes such as initiation of subduction [*Stern and Bloomer*, 1992]. Most plumes do not record evidence for melting past cpx-out. The most notable exceptions are the submarine glasses found on the flanks of the Kilauea Volcano, Hawaii [*Clague et al.*, 1991]. These are the most mafic plume-related glasses known, and phase-equilibria experiments [*Wagner and Grove*, 1998] indicate that they left behind a harzburgite residue. Melting at mid-ocean ridges does not appear to melt past cpx-out, nor does melting associated with continental rifting.

Grove, 1998]. However, to date, hydrous mantle melting experiments have not produced high SiO_2 melts, nor is there an existing numerical model that accurately predicts the composition of hydrous, mafic melts.

[4] Pioneering experimental studies over the last three decades have elucidated much about how melting occurs in the mantle [*Baker et al.*, 1995; *Falloon and Green*, 1987; *Falloon et al.*, 1988; *Hirose and Kushiro*, 1993; *Ito and Kennedy*, 1967; *Jaques and Green*, 1980; *Kinzler*, 1997; *Kinzler and Grove*, 1992a, 1992b, 1993; *Kushiro*, 1968; *Presnall et al.*, 1979; *Robinson et al.*, 1998; *Stolper*, 1980; *Takahashi et al.*, 1993; *Walter*, 1998]. These experimental studies of have typically focused on low-degree, anhydrous melting in an attempt to interpret MORB, and to a lesser extent ocean island basalt, melting conditions. Hydrous experimental data is less abundant [*Asahara and Ohtani*, 2001; *Falloon and Danyushevsky*, 2000; *Gaetani and Grove*, 1998; *Green*, 1976; *Hirose and Kawamoto*, 1995; *Kawamoto et al.*, 1996; *Kawamoto and Holloway*, 1997; *Kushiro*, 1968, 1972; *Mysen and Boettcher*, 1975]. Likewise, many of the existing numerical models that predict mantle melting conditions are not valid after cpx exhaustion and/or cannot incorporate the effects of H_2O [*Kinzler and Grove*, 1992a; *Mckenzie and Bickle*, 1988; *Niu and Batiza*, 1991]. Of the existing models, only the MELTS program predicts hydrous ol-opx-melt equilibria. Yet MELTS was not intended specifically for this purpose, and the errors in estimated melt composition and equilibrium temperatures are substantial [*Hirschmann et al.*, 1998b].

[5] In this study, we present a series of hydrous and anhydrous experiments aimed at constraining the composition of ol-opx saturated melts. The results are used to discuss the effect of H_2O on the activities of melt species, SiO_2 in particular. The experimental data, along with literature data, are also used to construct a semiempirical, partitioning based predictive melting model. For a given pressure, temperature and bulk composition (including H_2O content), the model estimates melt, ol and opx phase compositions as well as phase proportions. The model is primarily aimed at predicting the composition of hydrous melts in subduction zones, but can be applied to any melt that leaves behind a harzburgite residue, including picrites and komatiites.

2. Experimental Methods

2.1. Starting Compositions

[6] A primary goal of this study is to produce a numerical model that can predict the compositions of high-degree mantle melts based on experimentally produced mineral-melt equilibria. To provide the most leverage for the linear regression models, the starting compositions were chosen to produce ol-opx saturated melts over a wide range of P, T and H_2O conditions, rather than choosing only natural melts (Table 1). The first composition (BK2) is based on a least altered Barberton komatiite. Except for Na_2O, this is the same composition studied by *Parman et al.* [1997]. The Na_2O content of the original composition is too low to be in equilibrium with the clinopyroxene (cpx) found in the komatiite samples, and so has been increased to be consis-

Table 1. Starting Compositions[a]

	BK2	W	W3
SiO_2 (wt)	49.23	48.12	46.27
TiO_2	0.43	0.49	0.37
Al_2O_3	4.62	13.79	10.32
Cr_2O_3	0.34	0.25	0.19
FeO	11.13	8.48	8.80
MnO	0.2	0.13	0.10
MgO	23.14	18.72	26.40
CaO	10.14	8.73	6.53
Na_2O	0.61	1.10	0.82
K_2O	0.02	0.03	0.02
P_2O_5	0.05	0.23	0.17
NiO	0.14	0.02	0.01
Sum	100.1	100.1	100.0

[a]In weight percent.

Table 2. Experimental Results

Exp.	*P*, GPa	*T*, °C	Time, hours	Bulk H_2O	Melt	ol	opx	cpx	sp/gt	ol K_D	opx K_D	cpx K_D	H_2O Change	Σ residuals[2]
BK2.19	2.2	1400	31	6.0	92.1(4)[a]	0.4(2)	6.4(5)	–	tr[f]	0.335	0.301	–	–	0.015 (0.590)[e]
BK2.20	2.2	1350	57	6.0	75.9(7)[a]	4.1(6)	19.9(9)	–	tr[f]	0.355	0.307	–	–	0.108
BK2.24	1.5	1300	23	6.0	82.5(3)[b]	18.0(3)	–	–	–	0.325	–	–	–	0.088 (0.525)[e]
BK2.27	1.5	1450	26	0.0	56.5(9)	14.9(4)	–	28.3(10)	–	0.357	–	0.340	–	0.087
BK2.28	1.5	1500	48	0.0	82.4(9)	9.3(5)	6.9(12)	–	–	0.360	0.348	–	–	0.063 (2.183)[e]
BK2.30	1.5	1275	28	6.0	70.3(9)[b]	22.1(4)	0.8(6)	7.7(6)	–	0.332	0.302	0.275	–	0.214
W.7	1.2	1320	23	6.5	93.7(1)	5.85(1)	–	–	0.17(7)	0.337	–	–	0.07	0.076
W.9	1.5	1200	33	6.5	76.1(10)	10.2(10)	11.8(16)	–	0[c]	0.334	0.335	–	0.05	0.095 (2.429)[e]
W.10	1.5	1250	20	6.5	92.6(1)	7.6(1)	–	–	0.07(5)	0.355	–	–	0.10	0.051
W.11	1.5	1175	23	6.5	77.9(5)[b]	14.7(5)	8.0(8)	–	tr[f]	0.345	0.322	–	–	0.148
W.12	1.5	1175	31	6.5	64.7(4)	10.9(4)	19.9(6)	4.6(4)	tr[f]	0.335	0.322	0.313	−0.14	0.026
W.13	2.0	1200	21	6.5	61.7(14)[b]	–	30.9(6)	–	6.6(14)[d]	–	0.303	–	–	0.599
W.18	2.0	1300	28	6.5	91.9(8)[b]	–	7.4(7)	–	–	–	0.320	–	–	0.234
W.20	1.5	1400	76	0.0	68.1(8)	0[c]	31.2(7)	–	0.7(3)	–	0.321	–	–	0.202
W.21	2.0	1450	71	0.0	58.2(3)	–	28.8(2)	13.0(4)	0.17(5)	–	0.327	0.376	–	0.068
W.22	2.0	1250	26	6.5	85.1(15)[b]	4.9(12)	11.2(21)	–	tr[f]	0.348	0.328		–	0.198
W3.31	2.0	1300	24	6.4	70.5(5)	24.8(7)	3.5(6)	–	–	0.350	0.323	–	0.05	0.140
W3.32	2.0	1450	70	0.0	54.2(6)	19.4(4)	25.8(8)	–	–	0.336	0.331	–	–	0.034 (0.546)[e]
W3.33	2.0	1275	26	6.4	64.0(4)	24.2(3)	12.0(5)	–	–	0.339	0.319	–	0.12	0.167
W3.34	2.0	1425	94	0.0	23.6(9)	18.2(4)	29.8(8)	25.8(11)	tr[f]	0.327	0.307	0.352	–	0.028
W3.35	1.5	1450	67	0.0	71.6(4)	26.6(3)	0.9(5)	–	–	0.342	0.335	–	–	0.015 (1.340)[e]
W3.36	2.0	1475	72	0.0	62.3(6)	22.0(4)	15.7(8)	–	–	0.340	0.331	–	–	0.049

[a]These are remelted quench growth.
[b]Quench growth is analyzed by defocused beam (30 μm diameter).
[c]The phase is present in trace amounts (<2%), but the mass balance yields values that are negative or smaller than the associated errors.
[d]Aluminous phase is garnet.
[e]FeO is left out of mass balance. Value in parentheses is with FeO included.
[f]Trace, tr, i.e. too small to analyze.

tent with the 200 MPa clinopyroxene/melt Na_2O partitioning data. The second composition (W) is based upon a hydrous experimental melt in equilibrium with ol and opx reported by *Gaetani and Grove* [1998]. To promote saturation with harzburgite, the melt composition was reconstituted by adding 15 wt % ol and 15 wt % opx. A third composition (W3) was formed by adding 25 wt % Fo_{90} olivine to composition W. Both anhydrous and hydrous versions of these mixes were prepared. Hydrous mixes contained between 5.0 and 6.5 wt % H_2O (Table 2).

[7] All of the experimental starting compositions were prepared by mixing high-purity oxides. Iron was added as both Fe metal and Fe_2O_3 in the correct stoichiometric proportions to produce FeO. H_2O was added as $Mg(OH)_2$ (brucite). The brucite was prepared by placing MgO and H_2O in a pressure sealed Teflon beaker, which was placed inside an oven at 240°C for 48 hours. Weighing of the powder before and after indicated that ~96 wt % of the MgO was converted to $Mg(OH)_2$. Anhydrous powders were conditioned at log f_{O2} = QFM-1 for 24 hours at 1000°C. Hydrous powders could not be conditioned in this way because the process would dehydrate the powders. Their preexperiment f_{O2} was set by the oxidation state of Fe in the mix, which was entirely FeO. During the experiment, the f_{O2} was governed by the equilibrium between FeO in the melt and Fe in the AuPd capsule ($FeO^{melt} = Fe^{capsule} + 1/2O_2{}^{gas}$) [*Grove*, 1981]. The capsule was saturated with Fe at QFM-1 at 1 atm and activity calculations [*Borisov and Palme*, 2000] indicate that this was also the f_{O2} imposed during the experiment.

2.2. Experimental Procedures

[8] All experiments were performed in piston-cylinder devices at MIT using the hot piston in technique. Pressures for all devices have been calibrated to the Ca-Tschermakite (CATS) breakdown boundary [*Hays*, 1967], and pressures are considered accurate to 0.05 GPa. Temperature was measured with a W/Re thermocouple. The temperature gradient across the sample is estimated to be less than 10°C. For anhydrous experiments, sample powders were packed into graphite capsules. These were then placed into Pt capsules and welded shut. Hydrous sample powders were placed in $Au_{80}Pd_{20}$ capsules and welded shut [*Gaetani and Grove*, 1998]. These capsules were placed inside graphite capsules machined from graphite rod stock (Figure 2). In some experiments, the graphite outer capsule was replaced with MgO, with the result that ~50 wt % of the H_2O diffused out of the sample. With the graphite capsules, typical H_2O losses were 0–10 wt %, suggesting that the graphite is an effective barrier to H diffusion. The $Au_{80}Pd_{20}$ capsules were preconditioned with Fe before the high-pressure experiments. This was done by filling them with an andesite composition and placing them in a 1 atm furnace at log f_{O2} = QFM-1 and 1250°C for 72 hours. The silicate glass was then removed with a HF + nitric acid mixture. Fluoride residues after HF dissolution were first removed manually with a pick and then by soaking in HCl. The conditions and results of each experiment are given in Table 2.

3. Analytical Methods

[9] Experimental charges were analyzed with the JEOL 733 microprobes at the Massachusetts Inst. of Technology. Data were reduced with the CITZAF correction package using the atomic number correction of Duncumb and Reed, the absorption coefficients of Heinrich and the fluorescence correction of Reed [*Armstrong*, 1995]. The beam current

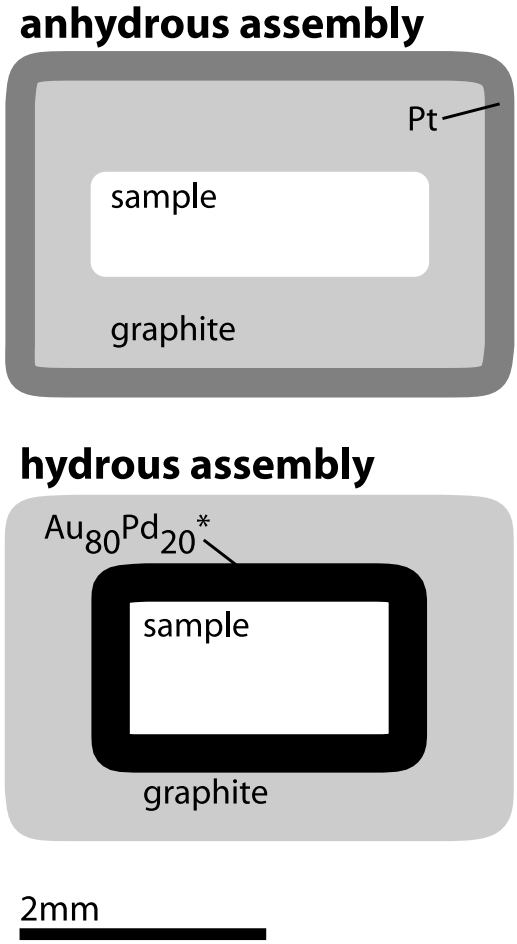

Figure 2. Experimental assemblies used in this study. For anhydrous experiments, the sample was placed in a graphite capsule, which was placed inside a Pt capsule and welded shut. For hydrous experiments, the sample was contained in an $Au_{80}Pd_{20}$ capsule presaturated with Fe [*Gaetani and Grove*, 1998]. This capsule was placed inside a graphite capsule.

was 10 nA with an accelerating voltage of 15 kV for all analyses. A 2 μm beam diameter was used for solid phases, a 20 μm beam for glass, and a 30 μm beam for "unquenched" melt. The term "unquenched" refers to melts that do not quench to a glass, but instead form a matrix of lathe shaped pyroxene with interstitial evolved melt. Because of the high MgO and H_2O contents of the melts studied here, and the high pressure and temperature of the experiments, the melts in only six of the hydrous experiments quenched to glass (W.7, W.9, W.10, W.12, W3.31, W3.34). Unquenched melts are typically analyzed by using a defocused beam or by rastering the beam of the microprobe. We have also followed this method. For each unquenched melt, we perform 30–40 analyses with the defocused beam. In two experiments, half of the melt quenched to glass and the other half did not. Analyses of both sides agree within error for all elements except Al_2O_3, which is slightly overestimated in the unquenched melt. In experiments BK2.19 and BK2.20 the melt and crystals were segregated enough to separate the quench growth from the crystals physically. The unquenched melt was placed in a Pt capsule and remelted in a 1 ATM furnace under air at 1300°C for ~20 min. The high f_{O2} prevents Fe loss to the Pt. These remelts were quenched into water and formed 100% glass. In both cases, the remelted glass composition was within the errors of the quench growth analyses, except for Al_2O_3. The compositions of all experimental products are given in Table 3. H_2O contents of melts that did not quench to glass were calculated using the phase proportion of the melt and the bulk H_2O content of the starting composition.

4. Results

4.1. Attainment of Equilibrium

[10] The experiments reported here are all synthesis experiments. No reversals have been performed. Although equilibrium has not been proven, it can be assessed by a number of means.

[11] 1. Loss or gain of mass to the enclosing capsule during the experiment inhibits equilibrium. All of our experiments have been mass balanced. Of the 22 experiments reported, all but 6 have sum of squared residuals (Σr^2) less than 0.25, indicating no significant diffusional exchange with the AuPd capsule. The remaining six clearly lost/gained Fe to the capsule. When FeO is left out of the mass balance, the sum r^2 for all six are below 0.1.

[12] 2. The Fe/Mg partitioning between olivine and melt, and between opx and melt are relatively independent of pressure and temperature. For magnesian-rich, alkali-poor melts, ol-melt $K_D^{Fe\text{-}Mg}$ should be 0.33 ± 0.03 and opx-melt $K_D^{Fe\text{-}Mg}$ should be 0.32 ± 0.03. Only experiments with K_D values within these ranges have been accepted. The six experiments with poor mass balances were included in the data set based on their acceptable K_D values, which suggest that Fe exchange with the capsule occurred early enough in the experiment for the solid phases to reequilibrate with the melt.

[13] 3. Experimental phases should be unzoned if they are in complete equilibrium. In reality, some zoning always persists, but only experiments where the zoning is small are accepted. The elements most likely to be lost are FeO and H_2O: FeO because it is soluble in the AuPd capsules of the hydrous experiments and H_2O because H atoms can rapidly diffuse through most materials. In practice, it is relatively easy to see when an experiment has been significantly affected by one of these mechanisms. FeO loss or gain shows up as strong FeO zoning in both ol and opx that is apparent in backscattered electron imaging. H_2O loss is apparent because of the strong effect it has on melting temperature. Experiments that lose H_2O are significantly more crystalline than successful hydrous experiments at the same conditions, and often have no melt present. In general, the high temperatures and/or high H_2O contents of the experiments, along with the relatively fast diffusion rates in ol and opx promote equilibrium. The excellent coherence of the experimental data (described below) is additional circumstantial evidence that equilibrium has been closely approached.

4.2. Phase Diagrams

[14] The anhydrous and H_2O-undersaturated phase diagrams for BK and W are shown in Figure 3. In addition, the melting point of Fe-conditioned $Au_{80}Pd_{20}$ is shown in

Table 3. Experimental Products[a]

Phase[b]	SiO_2	TiO_2	$Al2O_3$	Cr_2O_3	FeO*	MnO	MgO	CaO	Na_2O	K_2O	P_2O_5	NiO	H_2O	Sum[c]
							BK2.19							
Remelt	49.28(23)	0.44(1)	4.95(7)	0.26(2)	10.66(29)[d]	0.21(3)	22.50(12)	10.91(9)	0.60(8)	0.014(5)	0.06(2)	0.06(2)	5.43	*100.0*
ol	41.18(44)	0.00(1)	0.03(1)	0.09(1)	8.08(20)	0.11(1)	50.92(41)	0.19(2)	–	–	–	0.07(1)	–	100.7
opx	57.49(28)	0.01(1)	0.55(4)	0.41(4)	4.96(11)	0.11(2)	34.77(19)	1.52(5)	0.00(1)	–	–	0.03(1)	–	99.84
							BK2.20							
Remelt	47.35(44)	0.53(1)	6.15(7)	0.34(2)	11.3(36)	0.22(3)	19.04(14)	12.44(14)	0.79(6)	0.02(1)	0.07(1)	0.06(2)	6.58	99.40
ol	40.83(31)	0.01(1)	0.02(1)	0.11(1)	10.93(18)	0.16(1)	47.37(48)	0.22(2)	–	–	–	0.06(3)	–	99.72
opx	57.33(34)	0.03(1)	0.75(3)	0.48(2)	6.63(10)	0.17(1)	33.23(2)	2.2(3)	0.01(1)	–	–	0.05(1)	–	101.0
							BK2.24							
Quench	50.73(21)	0.51(2)	5.55(6)	0.42(4)	12.00(18)	0.21(2)	17.63(10)	12.34(10)	0.43(8)	0.09(2)	0.06(1)	0.03(2)	6.06	*100.0*
ol	40.82(25)	0.00(1)	0.02(1)	0.14(2)	10.57(22)	0.15(2)	47.78(48)	0.23(2)	–	–	–	0.07(1)	–	99.79
							BK2.27							
Quench	48.66(57)	0.74(5)	7.77(53)	0.32(4)	12.65(46)	0.21(3)	16.03(85)	12.8(21)	0.68(14)	0.05(2)	0.09(2)	0.01(2)	–	*100.0*
ol	40.16(33)	0.01(1)	0.06(1)	0.17(2)	13.03(11)	0.15(2)	46.25(47)	0.47(2)	–	–	-	0.05(2)	–	100.4
cpx	55.58(18)	0.07(1)	1.35(11)	0.59(4)	6.84(11)	0.18(3)	25.49(49)	9.89(44)	0.17(4)	–	–	–	–	100.2
							BK2.28							
Quench	50.38(18)	0.52(2)	5.74(4)	0.36(2)	9.86(21)	0.20(2)	19.76(11)	11.89(11)	0.57(6)	0.03(1)	0.06(1)	0.01(1)	–	99.39
ol	40.88(16)	0.00(1)	0.05(1)	0.18(1)	8.87(19)	0.12(2)	49.38(21)	0.35(3)	–	–	–	0.05(2)	–	99.89
opx	56.76(30)	0.03(1)	0.46(8)	0.39(4)	5.68(14)	0.16(2)	32.66(17)	3.33(12)	0.05(1)	–	–	–	–	99.53
							BK2.30							
Quench	50.76(89)	0.56(2)	6.47(10)	0.35(2)	12.59(42)	0.22(3)	15.73(23)	12.32(43)	0.87(11)	0.06(1)	0.06(2)	0.00(1)	7.11	*100.0*
ol	40.24(30)	0.03(1)	0.04(2)	0.10(1)	12.34(12)	0.15(2)	46.49(37)	0.22(1)	–	–	–	0.05(1)	–	99.65
opx	56.99(40)	0.04(1)	0.61(4)	0.6(5)	7.7(16)	0.18(3)	31.77(13)	2.21(13)	0.02(1)	–	–	–	–	100.1
cpx	54.81(47)	0.04(1)	0.74(4)	0.91(9)	4.51(15)	0.12(2)	20.5(22)	18.3(3)	0.18(2)	–	–	–	–	100.1
							W7							
Glass	48.78(25)	0.50(2)	14.7(9)	0.17(2)	8.23(16)	0.14(2)	16.8(7)	9.21(9)	1.16(4)	0.03(1)	0.23(3)	0.03(2)	7.40(35)	*100.0*
ol	41.4(37)	0.01(1)	0.05(2)	0.09(1)	8.17(8)	0.11(2)	49.46(35)	0.15(2)	–	–	–	0.01(1)	–	99.47
sp	0.15(1)	0.23(1)	24.70(30)	43.95(23)	12.94(16)	0.20(1)	17.25(27)	0.06(4)	–	–	–	0.03(2)	–	99.50
							W9							
Glass	49.17(28)	0.61(1)	17.58(12)	0.07(1)	6.89(14)	0.14(2)	12.82(9)	11.16(9)	1.12(3)	0.13(1)	0.22(1)	0.02(1)	8.96(47)	*100.0*
ol	41.11(55)	0.00(1)	0.05(1)	0.05(1)	8.99(16)	0.10(2)	50.02(77)	0.14(2)	–	–	–	0.05(2)	–	100.5
opx	54.81(40)	0.04(1)	4.58(33)	0.87(6)	5.9(12)	0.12(2)	32.79(31)	1.12(2)	0.02(1)	–	–	–	–	100.3
sp	0.23(17)	0.15(2)	40.95(12)	27.9(12)	12.14(27)	0.13(2)	18.65(64)	0.08(3)	–	–	–	0.01(1)	–	99.86
							W10							
Glass	48.58(21)	0.51(2)	14.89(5)	0.21(1)	8.63(16)	0.13(2)	16.18(9)	9.41(9)	1.13(5)	0.04(1)	0.26(2)	0.04(2)	7.76(26)	*100.0*
ol	40.84(22)	0.01(1)	0.06(1)	0.13(3)	9.22(19)	0.10(1)	48.77(45)	0.12(3)	–	–	–	0.02(2)	–	99.26
sp	0.15(1)	0.20(2)	28.49(72)	40.3(66)	13.1(17)	0.17(1)	17.54(27)	0.10(4)	–	–	–	–	–	100.0
							W11							
Quench	48.63(88)	0.65(6)	17.31(34)	0.08(1)	8.48(14)	0.12(2)	12.00(32)	11.01(15)	1.23(8)	0.09(1)	0.35(3)	0.04(2)	8.34	*100.0*
ol	40.21(33)	0.00(1)	0.04(1)	0.06(2)	11.39(9)	0.14(2)	46.74(25)	0.10(1)	–	–	–	0.04(3)	–	98.72
opx	53.95(16)	0.08(1)	4.49(25)	0.95(3)	7.07(9)	0.09(3)	31.11(17)	1.00(2)	0.00(1)	–	–	–	–	98.74
							W12							
Glass	47.63(27)	0.71(2)	18.85(1)	0.04(2)	8.40(18)	0.12(2)	10.48(6)	11.63(7)	1.72(8)	0.05(1)	0.34(1)	0.01(1)	8.69(39)	*100.0*
ol	39.66(23)	0.01(1)	0.06(4)	0.03(1)	12.53(20)	0.14(2)	46.66(16)	0.16(2)	–	–	–	0.05(2)	–	99.31
opx	53.24(45)	0.09(1)	6.38(29)	0.41(8)	7.8(10)	0.13(2)	30.21(27)	1.34(7)	0.02(1)	–	–	–	–	99.61
cpx	51.52(27)	0.18(1)	5.68(32)	0.37(5)	4.36(14)	0.07(2)	17.36(18)	19.62(38)	0.35(4)	–	–	–	–	99.54
							W13							
Quench	46.61(90)	0.68(2)	17.15(4)	0.08(2)	9.57(15)	0.12(2)	12.61(51)	11.52(18)	1.22(12)	0.08(1)	0.34(1)	0.02(1)	10.53	*100.0*
opx	53.85(33)	0.06(1)	5.43(3)	0.52(9)	7.19(13)	0.12(2)	31.29(39)	1.2(7)	0.01(1)	–	–	–	–	99.68
gt	41.29(28)	0.13(1)	22.82(21)	1.38(9)	7.96(14)	0.21(3)	19.09(37)	6.7(11)	0.01(1)	–	–	–	–	99.58
							W18							
Quench	48.09(17)	0.5(1)	14.55(8)	0.17(2)	8.5(13)	0.11(2)	17.35(9)	9.37(9)	1.00(10)	0.11(2)	0.23(2)	0.01(1)	7.07	*100.0*
opx	55.25(38)	0.04(1)	3.91(22)	0.96(6)	5.31(10)	0.10(5)	33.82(28)	0.83(1)	0.02(1)	–	–	–	–	100.2
							W20							
Glass	46.43(34)	0.69(1)	16.76(9)	0.08(2)	8.83(19)	0.12(2)	13.27(14)	11.85(10)	1.25(7)	0.06(1)	0.35(2)	–	–	99.70
opx	53.03(40)	0.09(1)	6.47(13)	0.50(2)	6.51(6)	0.08(1)	30.44(24)	2.21(5)	0.06(2)	–	–	–	–	99.39
sp	0.28(4)	0.10(2)	61.87(64)	7.43(16)	8.47(21)	0.06(2)	21.64(64)	0.05(1)	–	–	–	0.02(2)	–	99.92
							W21							
Glass	45.99(23)	0.77(2)	16.76(10)	0.09(3)	9.78(14)	0.12(2)	13.09(8)	11.29(10)	1.28(9)	0.06(1)	0.40(2)	0.01(1)	–	99.65

Table 3. (continued)

Phase[b]	SiO_2	TiO_2	$Al2O_3$	Cr_2O_3	FeO*	MnO	MgO	CaO	Na_2O	K_2O	P_2O_5	NiO	H_2O	Sum[c]
opx	51.06(36)	0.09(1)	9.12(26)	0.46(2)	7.09(1)	0.09(2)	29.00(20)	2.27(6)	0.1(1)	–	–	–	–	99.28
cpx	50.78(41)	0.13(2)	9.83(29)	0.50(2)	5.88(17)	0.11(2)	20.9(39)	11.68(49)	0.52(4)	–	–	–	–	100.3
sp	0.35(3)	0.09(1)	62.87(59)	4.74(8)	9.1(10)	0.06(2)	22.07(25)	0.16(1)	–	–	–	0.01(1)	–	99.45
							W22							
Glass	46.98(34)	0.57(2)	16.77(38)	0.11(3)	8.96(14)	0.13(2)	15.27(23)	10.00(16)	0.87(10)	0.08(2)	0.26(2)	0.00(1)	8.1(13)	*100.0*
ol	41.00(25)	0.02(1)	0.05(1)	0.05(1)	10.01(21)	0.09(2)	48.99(21)	0.11(1)	–	–	–	0.01(1)	–	100.3
opx	55.04(53)	0.06(1)	4.72(10)	0.83(1)	6.24(26)	0.12(3)	32.41(23)	0.96(8)	0.02(1)	–	–	–	–	100.0
							W3.31							
Glass	48.10(27)	0.50(2)	14.65(15)	0.17(4)	8.99(20)	0.06(6)	17.3(14)	8.75(14)	1.03(6)	0.03(2)	0.32(4)	0.10(4)	7.43(38)	*100.0*
ol	40.85(59)	0.00(1)	0.05(2)	0.07(1)	9.01(23)	0.08(3)	49.56(42)	0.12(1)	–	–	–	0.10(2)	–	99.84
opx	55.44(53)	0.05(1)	3.63(24)	0.83(1)	5.61(13)	0.08(1)	33.40(5)	0.79(3)	0.02(2)	–	–	–	–	99.85
							W3.32							
Glass	45.47(48)	0.63(2)	15.50(20)	0.11(4)	8.76(17)	0.08(5)	16.03(15)	11.22(11)	1.34(8)	0.02(2)	0.43(4)	0.14(5)	–	99.73
ol	40.71(28)	0.01(1)	0.18(6)	0.08(1)	9.14(16)	0.08(3)	49.72(41)	0.27(1)	–	–	–	0.08(1)	–	100.3
opx	53.45(35)	0.08(1)	6.95(40)	0.43(3)	5.66(19)	0.09(2)	31.28(18)	1.91(5)	0.09(1)	–	–	–	–	99.93
							W3.33							
Glass	46.55(28)	0.57(2)	15.71(13)	0.11(2)	9.48(19)	0.10(7)	15.60(13)	10.22(12)	1.15(8)	0.03(2)	0.37(4)	0.11(5)	8.73(60)	*100.0*
ol	40.47(36)	0.01(1)	0.05(1)	0.05(2)	10.03(13)	0.1(2)	48.71(39)	0.13(2)	–	–	–	–	–	99.65
opx	54.47(35)	0.05(1)	4.82(24)	0.76(11)	6.28(21)	0.09(2)	32.42(31)	0.95(3)	0.02(2)	–	–	–	–	99.87
							W3.34							
Quench	43.88(49)	1.04(3)	15.36(19)	0.06(3)	10.97(25)	0.06(3)	13.45(20)	11.09(10)	2.19(15)	0.08(3)	0.71(2)	0.14(5)	–	99.04
ol	39.5(0)	0.02(2)	0.16(2)	0.05(1)	12.49(17)	0.10(2)	46.88(47)	0.28(2)	–	–	–	0.08(1)	–	99.57
opx	52.32(70)	0.13(1)	8.19(54)	0.22(2)	7.32(13)	0.11(2)	29.26(34)	2.18(7)	0.13(1)	–	–	–	–	99.85
cpx	50.99(23)	0.21(3)	8.90(42)	0.24(2)	5.89(23)	0.11(3)	20.51(49)	12.46(45)	0.60(4)	–	–	–	–	99.90
							W3.35							
Glass	48.60(25)	0.48(3)	14.36(12)	0.15(3)	7.70(15)	0.06(3)	17.82(14)	8.98(22)	1.02(10)	0.02(1)	0.20(6)	0.01(1)	–	99.41
ol	41.34(23)	0.0	0.14(1)	0.10(1)	7.42(10)	0.05(2)	50.26(59)	0.23(1)	–	–	–	0.00(1)	–	99.55
opx	55.25(55)	0.07(1)	4.02(58)	0.52(6)	4.81(17)	0.03(2)	33.18(49)	1.26(8)	0.03(1)	–	–	–	–	99.17
							W3.36							
Glass	46.47(37)	0.56(2)	14.68(16)	0.13(2)	9.55(16)	0.08(2)	17.00(18)	10.01(10)	1.13(11)	0.03(1)	0.28(3)	0.01(1)	–	99.94
ol	40.29(36)	0.00(1)	0.18(2)	0.09(2)	9.4(20)	0.07(2)	49.22(30)	0.26(1)	–	–	–	–	–	99.50
opx	53.94(52)	0.08(1)	6.44(62)	0.45(4)	5.83(8)	0.04(4)	31.32(21)	1.6(7)	0.07(1)	–	–	–	–	99.77

[a]Dash indicates the element was not analyzed. Standard deviation of last digit given in parentheses. Read 49.28(23) as 49.28 ± 0.23.

[b]Remelt, remelted quench growth; quench, quench growth analyzed by defocused beam (30 μm diameter); ol, olivine; opx, orthopyroxene; cpx, clinopyroxene; sp, spinel; gt, garnet. All concentrations are in weight percent.

[c]For glass and solid phases, analytical totals are given. For quench and hydrous glasses, analyses are summed to 100 (italics). H_2O contents of glass are by summation deficit. H_2O contents of quench calculated assuming no H_2O loss (= H_2O_{bulk}/F_{melt}). FeO* indicates that all Fe assumed to be Fe^{2+}.

[d]FeO from analyses of quench growth. Remelting on Fe-saturated loop increased Fe content of glass.

Figure 3a. A few hydrous experiments were performed in unconditioned capsule to extend the hydrous experiments to higher temperatures (experiments above the Fe-saturated $Au_{80}Pd_{20}$ melting line). While the Fe loss was too great to allow them to be used in the chemical modeling, they have been used to place additional constraints on the phase boundaries. Because of the Fe loss, we have not included these experiments in Table 2 or 3. The data are available upon request.

[15] Under anhydrous conditions, olivine is on the liquidus of composition BK2 up to ~1.5 GPa and 1500°C. At which point, opx becomes the liquidus phase. The exact multiple saturation point is not bracketed, but the experiment (BK2.24) at 1.5 GPa is quite close to the liquidus (83% melt) and is saturated with both ol (9%) and opx (7%). As opx enters the melt in greater proportion, the multiple saturation point should be at slightly higher pressure and temperature than the experiment.

[16] With 5 wt % H_2O in the BK2 bulk composition, the phase boundary for ol is lowered by ~100°C at 1.5 GPa, decreasing to 50°C at 2.4 GPa. The slope of the ol phase boundary is slightly greater than the slope of the $Au_{80}Pd_{20}$ melting point, limiting the pressures at which ol-opx saturated melts could be produced to less than 2.6 GPa. The opx phase boundary is lowered by over 200°C, causing the ol-opx saturation point to move to higher pressure and lower temperature (~2.3 GPa and 1450°C), relative to anhydrous conditions. Cpx becomes a stable phase 100°C below the opx phase boundary.

[17] Under anhydrous conditions, ol is on the liquidus of composition W until ~1.3 GPa, after which opx is on the liquidus. The multiple saturation point is at ~1350°C, though this is not well bracketed. The first appearance of cpx is 50°C below the opx phase boundary. With 6.5 wt % H_2O, the ol and opx boundaries are depressed by 100–150°C. The cpx stability is lowered by ~150°C. In the hydrous experiments, cpx becomes unstable somewhere between 1.5 and 2.0 GPa, at which point garnet becomes stable. The stability of garnet at such low pressures is due to the low temperatures of the hydrous experiments and has

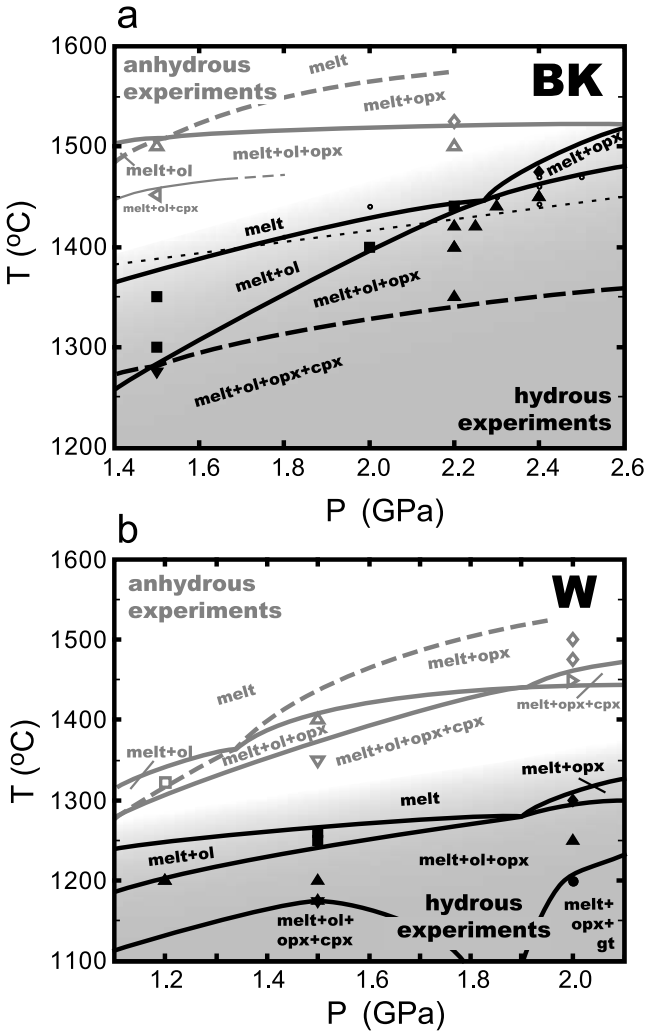

Figure 3. Experimentally determined phase diagrams under anhydrous and H_2O-undersaturated conditions. (a) Phase diagram for a Barberton komatiite composition (BK2, Table 1). (b) Phase diagram for composition W (Table 1). Anhydrous experiments and phase boundaries are dark gray. Hydrous experiments and phase boundaries are black. Thick dashed lines indicate phase boundaries that are not bracketed by experiments but inferred using the phase proportions of the nearest experiments. Experimental phase assemblages are indicated by symbol: melt + ol (square), melt + opx (diamond), melt + ol + opx (triangle), melt + ol + opx + cpx (inverted triangle), melt + opx + gt (circle). Small open circles indicate experiments in which the Fe-saturated $Au_{80}Pd_{20}$ capsule melted. Thin dashed line indicates the inferred melting point of Fe-saturated $Au_{80}Pd_{20}$. Unsaturated $Au_{80}Pd_{20}$ capsules were used for hydrous experiments above this line and are only used here to infer phase relations. Note the large effect of H_2O to lower the temperature of the opx boundary (~200°C) versus the smaller (~100°C) drop in the ol-out boundary. Because of the different slopes of the two boundaries, this results in the melt + ol + opx liquidus saturation point moving to higher pressures and lower temperatures in the hydrous experiments.

been observed in previous hydrous experimental studies [*Gaetani and Grove*, 1998].

4.3. Melt Reactions

[18] Pairs of experiments separated by 50°C or less have been used to estimate melting reactions (Table 4). Both wet and dry experiments show that opx dominates the solid input to the melt. For compositions BK2 and W, the ratio of opx to ol entering the melt is ~4:1. For composition W3, the melting is incongruent and ol is produced. H_2O appears to have little effect on the melting coefficients, as both wet and dry W3 experiments have very similar coefficients for both ol and opx.

4.4. Mineral/Melt Partitioning

[19] The effect of water on phase equilibria can be evaluated by examining the mineral/melt partition coefficients (D). At equilibrium,

$$\mu_a^i = \mu_b^i \tag{1}$$

$$\mu_a^{i,0} + RT \ln a_a^i = \mu_b^{i,0} + RT \ln a_b^i \tag{2}$$

where μ_a^i is the chemical potential of component i in phase a, $\mu_a^{i,0}$ is the standard state chemical potential, R is the gas constant, T is temperature, and a_a^i is the activity of component i in phase a. Activity is related to composition by

$$a_a^i = \gamma_a^i x_a^i, \tag{3}$$

where x_a^i is mole fraction and γ_a^i is the activity coefficient of component i in phase a. Substituting equation (3) into equation (2), and solving for the solid/melt D value yields

$$\ln D^{\text{solid/melt}} = \Delta\mu_i^{a-b}/RT + \ln\left(\gamma_b^i/\gamma_a^i\right), \tag{4}$$

where D is the ratio of the mole percent of an element in the solid to its mole percent in the melt. If mixing of an element in the crystal and melt follows Raoult's law (γ = 1) or Henry's law (γ = constant), then plots of ln D versus $1/T$ should produce straight lines. Conservative single cation oxide components (e.g., MgO, $AlO_{1.5}$, $HO_{0.5}$) are used in all regressions.

[20] For FeO and MgO in both ol and opx, ln D shows an excellent correlation with $1/T$, suggesting that the activity coefficients for these elements are nearly constant. The data for opx are shown in Figure 4. No difference is seen between the hydrous and anhydrous experiments, implying that H_2O has little effect on the activity coefficients of FeO and MgO in the liquid. Neither is there a difference between experiments with different starting compositions, as all of the data fall on the same lines. The tightness of the lines is a good indication that the experiments have closely approached equilibrium, while the parallel slopes of the FeO and MgO lines for both ol and opx indicate that near constant Fe/Mg K_D have been maintained. Previous studies [*Gaetani and Grove*, 1998] have observed similar systematics in ol-opx-cpx saturated melts.

[21] The D values for SiO_2 do not display Arrehnius relationships in either ol or opx (Figure 5a). D SiO_2 for both ol and opx are distinctly higher when H_2O is present.

Table 4. Melt Reactions

Experiment Pair	P (GPa)	H_2O (wt.%)	T1–T2 (°C)	Melt[a]	ol[a]	opx[a]	Σ res[2b]
BK2.19–BK2.20	2.2	5.0	1400–1350	1.00(1)	−0.23(1)	−0.87(1)	0.14
W.10–W.9	1.5	6.5	1250–1200	1.00(1)	−0.17(1)	−0.71(1)	0.024(3.35)[c]
W3.31–W3.33	2.0	5.0	1300–1275	1.00(1)	0.25(1)	−1.26(2)	0.17
W3.36–W3.32	2.0	0.0	1475–1450	1.00(1)	0.29(1)	−1.22(1)	0.016(1.39)[c]

[a]Amount of phase produced by raising temperature from T2 to T1, normalized to 1 unit of melt produced. Positive numbers indicate phase percentage increase. Values determined by mass balancing the melt from low temperature experiment and the average of the solid phase compositions from both experiments with the composition of the high temperature melt. All calculations are done on an anhydrous basis. Numbers in parentheses are errors on last digit from linear regression.

[b]Sum of residual errors to linear fit regression.

[c]FeO is left out of regression. Values in parentheses are regression with FeO included.

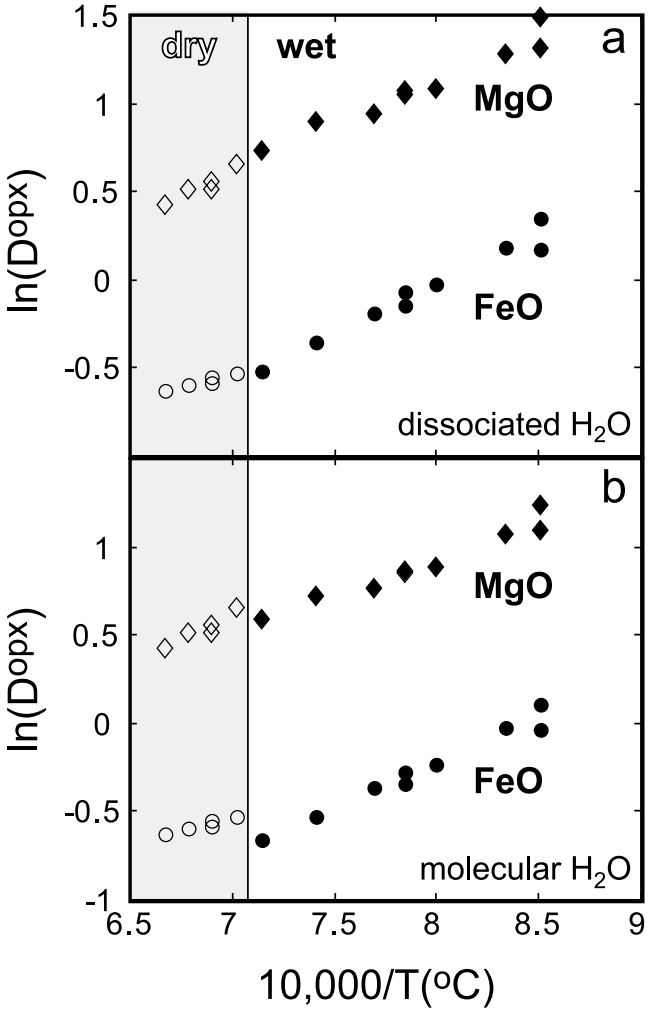

Figure 4. Ahrennius plots of FeO (circles) and MgO (diamonds) partitioning between opx and melt produced in experiments (Tables 2 and 3). (a) Partition coefficients calculated assuming that all H_2O was dissociated (OH^-). Both anhydrous (open symbols) and hydrous data (solid symbols) follow linear trends. There is a small change of slope between the wet and dry FeO partitioning data. (b) Partition coefficients calculated assuming that all H_2O was molecular (H_2O). A significant break occurs between the hydrous and anhydrous data. This suggests that dissolved H_2O is predominantly dissociated in mafic melts.

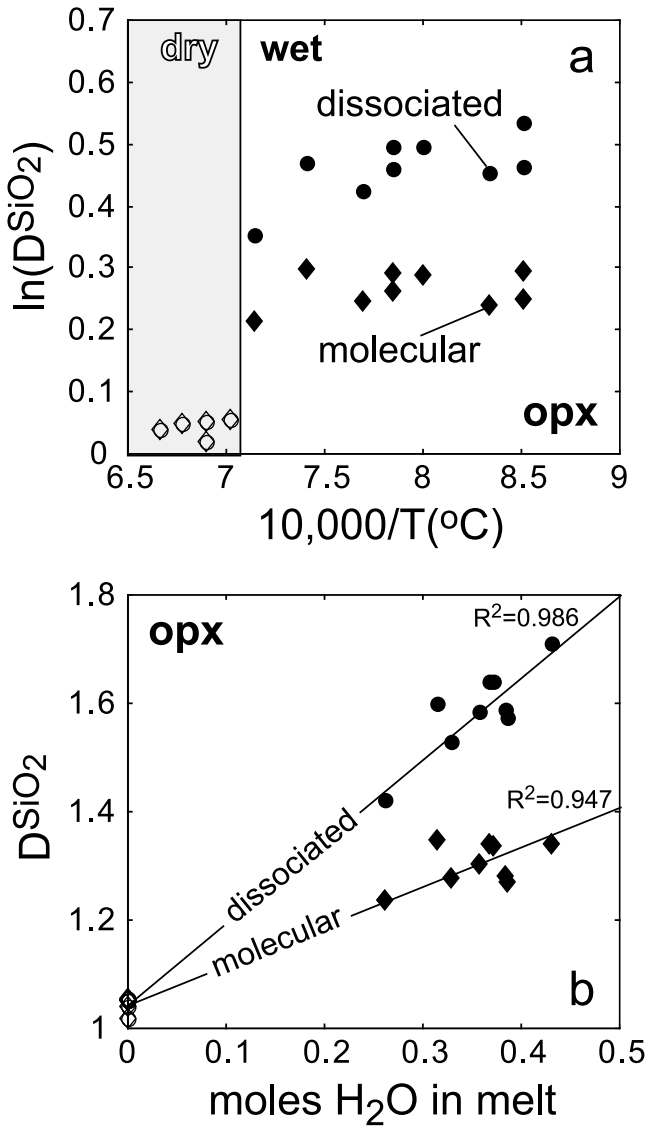

Figure 5. Partitioning of SiO_2 between opx and melt in anhydrous (open symbols) and hydrous (closed symbols) experiments. (a) Partition coefficients versus inverse temperature. No linear relationship is seen in the Ahrennius plot whether dissolved H_2O is assumed to be dissociated (circles) or molecular (diamonds). (b) A linear trend between D_{SiO2} and H_2O. The R^2 of the linear fits is slightly better when the dissolved H_2O is assumed to be dissociated (R^2 = 0.986) than when it is assumed to be molecular (R^2 = 0.947).

However, when H_2O is removed from the hydrous melt compositions, the SiO_2D values are the same as in the anhydrous experiments (ln (D) = 0.03 ± .02). This suggests that H_2O is not mixing with SiO_2 in the same manner as with MgO and FeO. Following *Bottinga* [1972], *Drake* [1976] proposed a two-lattice model for melts in which the network forming melt species (SiO_2, $CaAl_2O_4$, $NaAlO_2$, etc.) and network modifiers (MgO, FeO, CaO, etc.) form separate lattice sites. Species of the same type mix nearly ideally, but mixing does not occur between the two lattice sites. The partitioning data indicate that H_2O is mixing nearly ideally with the network modifiers, producing the Arrehnius relationships for MgO and FeO (Figure 4), but is not mixing with SiO_2 on the network-forming lattice site. Assuming H_2O does mix on the SiO_2 lattice site (Figure 5a) produces artificial breaks between the hydrous and anhydrous partitioning data. It also produces a somewhat misleading correlation between H_2O and SiO_2 partitioning (Figure 5b).

4.5. H_2O Speciation

[22] The speciation of H_2O in the melt can be examined with the partitioning data. *Burnham* [1975] proposed that the linear relationship between the fugacity of H_2O and the square of the H_2O concentration in experimental melts implies that all H_2O is dissolved as OH in silicate melts. Stolper demonstrated that silicate glasses contained significant amounts of molecular H_2O [*Stolper*, 1982a, 1982b]. He proposed that the OH/H_2O ratios in the glasses were indicative of the ratios in the melts from which they were quenched and also that this speciation could also produce the observed relationship between H_2O fugacity and concentration. Subsequent in situ analyses of H_2O speciation in melts have determined H_2O speciation in melts directly. These studies show a steep temperature dependence to the OH/H_2O ratio [*Ihinger et al.*, 1999; *Shen and Keppler*, 1995; *Withers et al.*, 1999]. Extrapolation of these observed OH/H_2O ratios to the temperature of our mantle melting experiments indicates that nearly all H_2O should be present as OH. The high molecular H_2O in rhyolitic glasses records the speciation of H_2O of the melt at the glass transition, which occurs at low (600–700°C) temperatures [*Dingwell and Webb*, 1990].

[23] When the experimentally determined D values for the network modifiers are calculated assuming all H_2O as $HO_{0.5}$, linear trends are observed for MgO and FeO partitioning (Figure 4). When treated as all molecular H_2O, a distinct break occurs between the hydrous and anhydrous data. The same break occurs in ol-opx-cpx saturated partitioning data [*Gaetani and Grove*, 1998, Figure 5]. In addition, a slightly better linear correlation is found between D SiO_2 and H_2O concentration (Figure 5b) when H_2O is treated as predominantly dissociated instead of molecular. The partitioning data corroborate Burnham's model and in situ observations that H_2O predominantly dissolves as OH at high temperatures.

5. Activity of Silica in Hydrous Melts

5.1. Temperature and Compositional Effects

[24] The activity of silica in ol-opx saturated melts is controlled by the reaction:

$$SiO_2^{melt} + Mg_2SiO_4^{ol} = Mg_2Si_2O_6^{opx} \quad (5)$$

and activity values can be calculated using

$$\Delta G^o = RT \ln K = RT \ln\left[a_{en}^{opx} / \left(a_{SiO2}^{melt} * a_{fo}^{ol}\right)\right] \quad (6)$$

where ΔG^o is the difference in standard state energies between the product and reactants, R is the gas constant, T is temperature (in kelvin), a_{en}^{opx} is the activity of clinoenstatite in orthopyroxene, a_{SiO2}^{melt} is the activity of SiO_2 in the melt, and a_{fo}^{ol} is the activity of forsterite in olivine. The MELTs supplemental calculator [*Asimow and Ghiorso*, 1998; *Ghiorso and Sack*, 1995] has been used to calculate these values for the experimentally produced ol, opx, and melts in this study as well as from the literature [*Gaetani and Grove*, 1998; *Hesse and Grove*, 2002; *Kinzler*, 1997; *Parman et al.*, 1997; *Walter*, 1998].

[25] The largest effect on γ_{SiO2}^{melt} is the MgO and SiO_2 content of the melt (Figure 6a). The three compositions used in this study and those used by *Gaetani and Grove* [1998] produce well separated trends with slopes that are identical within the associated errors. The values for ln γ_{SiO2}^{melt} for the most MgO-rich composition (BK2) approach the value of ~0.45 for a pure MgO-SiO_2 liquid saturated with ol and opx [*Ryerson*, 1985]. Alkalis, aluminates and other melt composition parameters affect γ_{SiO2}^{melt} as well [*Hirschmann et al.*, 1998a], but these effects are small relative to the effects of MgO and SiO_2 in this data set, especially the highly mafic compositions. Some of the scatter about the trends in Figure 6 may be the result of variations in these melt compositional parameters.

[26] Inverse temperature correlates with ln γ_{SiO2}^{melt} (Figure 6a), but has the opposite slope from that derived from thermodynamic properties [*Ryerson*, 1985]. In fact, the trend in Figure 6a is due to the correlation between equilibrium temperature and the H_2O content of the melt. When plotted against H_2O content, the correlation with ln γ_{SiO2}^{melt} is improved (Figure 6b). The activity coefficients were calculated assuming simple melt components, such that the higher the H_2O content of the melt, the lower the SiO_2 concentration becomes. Yet if *Drake* [1976] is correct and network modifiers such as H_2O do not mix with network formers such as SiO_2, then the activity coefficient of SiO_2 should be independent of the H_2O content of the melt. This can be tested by removing H_2O from the melt and recalculating the activity coefficients (Figure 6c). When this is done, the data again form parallel trends versus inverse temperature, but unlike in Figure 6a, they agree precisely with the predicted temperature dependence of γ_{SiO2}^{melt} [*Ryerson*, 1985]. While not a fully thermodynamic analysis, the correlation indicates that the primary effect of H_2O on silica activity coefficients is thermal and that correlations with melt H_2O content are the result of the melt components chosen.

[27] Pressure causes γ_{SiO2}^{melt} to decrease slightly (Figure 6). The effect does not appear to be linear. The difference between melts at 2.0 GPa and 1.5–1.6 GPa is barely detectable while the change from 1.6 to 1.2 GPa in the Gaetani and Grove experiments is significantly larger. The decreasing effect at higher pressures is consistent with thermodynamic expressions for the pressure dependence of silica activity [*Carmichael*, 2002].

[28] Apparent relationships between the activity coefficient of silica and melt composition can be produced if the

effects of H_2O, temperature and pressure are not addressed. For instance, *Carmichael* [2002] has proposed that RT ln γ_{SiO2}^{melt} increases as MgO decreases. This is opposite of the general conception that ideality should be approached as melts become more mafic and the equilibrium temperatures rise (Figure 6). In fact, the correlation found by Carmichael is the result of comparing high-MgO melts produced at 1.2–2.0 GPa with low-MgO melts produced at much lower experimental pressures (Figure 7). The mafic melts have lower RT ln γ_{SiO2}^{melt} in large part because they are at higher pressures, not because of their higher MgO contents. By comparing experiments at the same pressures, it is evident that RT ln γ_{SiO2}^{melt} does increase with MgO content as expected (Figure 7a).

[29] Similarly, Carmichael proposed that RT ln γ_{SiO2}^{melt} increases with increasing $Na_2O + K_2O$ concentration in the melt [*Carmichael*, 2002], opposite what previous studies have found [*Hirschmann et al.*, 1998a]. When melts with $Na_2O + K_2O < 0.25$ are compared, the expected negative correlation is found between alkalis and RT ln γ_{SiO2}^{melt} (Figure 7b). Experiments with $Na_2O + K_2O > 0.25$ do not fall on this trend and are offset to higher RT ln γ_{SiO2}^{melt}, apparently reversing the trend seen in the lower alkali melts. More experiments with high alkali melts are needed to constrain these trends better, but it does appear that for high alkali melts, RT ln γ_{SiO2}^{melt} increases with alkalis. However, for the majority of mantle melts (with $Na_2O + K_2O < 0.25$), the opposite trend applies.

5.2. Origin of High SiO_2 in Hydrous Melts

[30] It is a long-standing observation that hydrous magmas are silica-rich relative to anhydrous magmas, and so hydrous subduction-related magmas are quartz-normative (andesitic) while anhydrous mid-ocean ridge magmas are olivine-hypersthene to nepheline normative (basaltic) [*Gill*, 1981]. This is typically attributed to the depolymerization of SiO_2 chains in the melt, which stabilize depolymerized orthosilicate components such as olivine, over chain or framework silicate melt components, in which the SiO_2 tetrahedra are more linked [*Kushiro*, 1972]. The expansion of the olivine stability field causes the melts to become more silica-rich. However, hydrous experiments, including those in this study, have failed to produce melts with high enough SiO_2 to reproduce andesite compositions, when the melts are compared on a volatile-free basis. When H_2O is left in the melt composition, there is little shift of the ol-opx boundary and there is no increase of SiO_2 in the hydrous

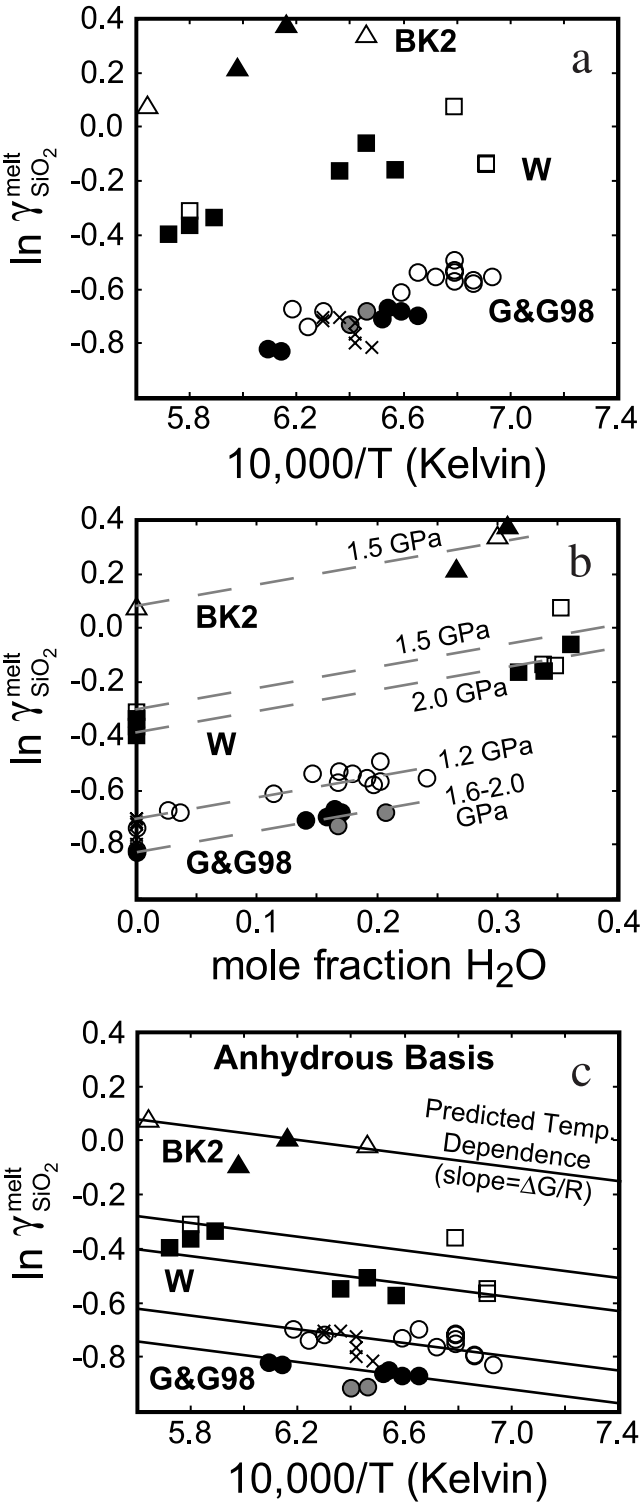

Figure 6. Activity coefficients for hydrous and anhydrous experimental melts in equilibrium with ol and opx from this study and from literature data [*Gaetani and Grove*, 1998; *Kinzler*, 1997]. (a) Activity coefficient versus inverse temperature. The experimental compositions G&G98 (circles, open for 1.2 GPa, solid for 1.6 GPa, and gray for 2.0 GPa), W (squares, open for 1.5 GPa and solid for 2.0 GPa) and BK2 (triangles, open for 1.5 GPa and solid for 2.2 GPa) produce separate trends with the same slope. High-pressure experiments (>1.6 GPa) consistently have lower activity coefficient values than lower-pressure (<1.6 GPa) data, providing evidence for a pressure effect. Anhydrous experiments of *Kinzler and Grove* [1992a] at 1.2 GPa shown as a cross. These data were used by *Gaetani and Grove* [1998] to deduce the effect of temperature on silica activity coefficients. (b) Activity coefficient versus melt H_2O content. The correlations are slightly better than against $1/T$, and the difference between the high- and low-pressure experiments is clearer. (c) Activity of silica corrected for dilution by H_2O versus inverse temperature. Lines indicate theoretical temperature dependence of silica activity coefficient [*Ryerson*, 1985].

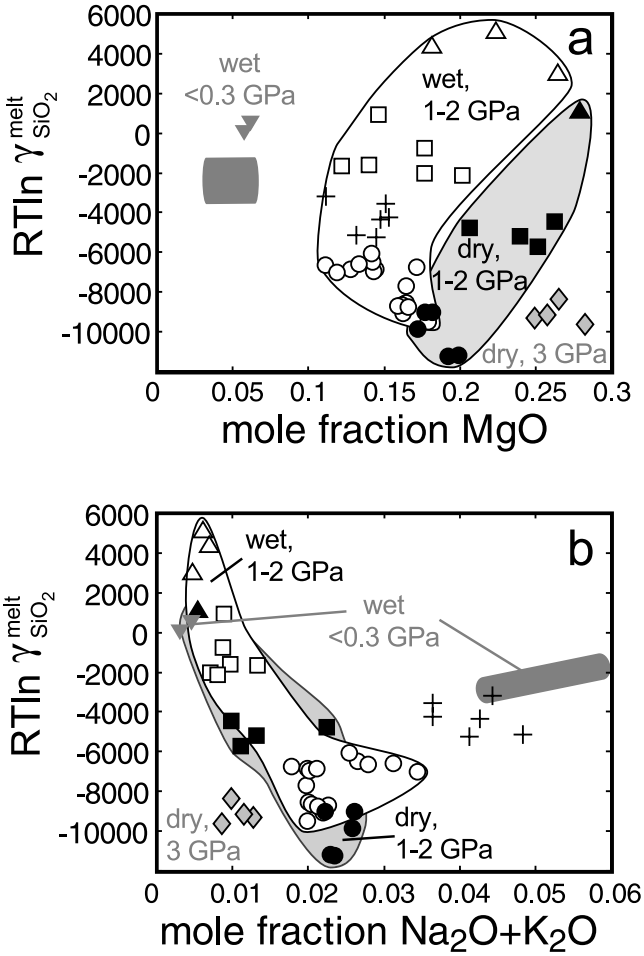

Figure 7. *RT* ln $\gamma^{melt}_{SiO2\,versus}$ melt composition for W&W3 (squares, this study), BK2 (triangles, this study), hydrous lherzolite melts at 1–2 GPa (circles, *Gaetani and Grove* (1998)), anhydrous lherzolite melt at 3 GPa (diamonds, *Walter* [1998]), alkali-rich mantle melts (crosses, *Hesse and Grove* [2002]), fractionated komatiite at 0.2 GPa (inverted triangles, *Parman et al.* [1997]), and andesites at <0.3 GPa (gray areas, *Carmichael* [2002]). (a) *RT* ln γ^{melt}_{SiO2} of hydrous (solid symbols) and anhydrous (open symbols) melts versus melt MgO contents. When hydrous or anhydrous experiments at similar pressures are compared, the trend is clearly for *RT* ln γ^{melt}_{SiO2} to increase with increasing MgO. (b) *RT* ln γ_{SiO2} of hydrous (solid symbols) and anhydrous (open symbols) melts versus melt alkali (Na_2O + K_2O) contents. The hydrous and anhydrous data at 1–2 GPa largely overlap, indicating that there is little correlation between H_2O and alkalis. While the 3 GPa data [*Walter*, 1998] have lower *RT* ln γ^{melt}_{SiO2} than the 1–2 GPa data, the 0.2 GPa komatiite data [*Parman et al.*, 1997] overlap the 1–2 GPa data. The alkali-rich experiments at both high- [*Hesse and Grove*, 2002] and low-pressure [*Carmichael*, 2002] show slightly elevated *RT* ln γ^{melt}_{SiO2}.

melts [*Gaetani and Grove*, 1998]. The apparent expansion of the olivine stability field is a result of comparing melts on an anhydrous basis. The question then remains, if H_2O does not increase the SiO_2 content of mantle melts, then why are subduction zone magmas andesitic?

[31] The analysis of the effects of H_2O on silica activity coefficients described above offers a potential explanation. When compared on an anhydrous basis, γ^{melt}_{SiO2} varies only slightly with temperature (Figure 6c). Likewise, mineral-melt partition coefficients for SiO_2 vary little when compared on an anhydrous basis (Figure 8). This is the essential effect of ol and opx buffering the activity of SiO_2. The partition coefficient for MgO, on the other hand, changes tremendously over the same temperature range (Figure 8), as the activity of MgO is not buffered. Therefore, at low temperatures, the concentration of MgO (and FeO) decreases in the melt while the concentration of SiO_2 is maintained by the ol-opx buffer (by dissolving opx and precipitating ol). The overall effect is to increase the SiO_2/(MgO + FeO) ratio in the melt at low temperatures.

[32] The failure of experiments to reproduce the high SiO_2 contents of subduction-related andesites may be because they were performed at higher temperatures than those at which most andesites last equilibrated with the mantle. Most hydrous mantle melting experiments have contained 3–7 wt % H_2O and have been run at temperatures above 1200°C, producing melts with 49–52 wt % SiO_2 (anhydrous basis). These results have reproduced the compositions of basaltic andesites with <54 wt % SiO_2 [*Baker et al.*, 1994]. The higher SiO_2 contents of mafic andesites (>6 wt % MgO, >54 wt % SiO_2) may indicate equilibration at lower temperatures (1000–1100°C) and higher H_2O (>7 wt %) contents than existing experiments. Some petrologic studies of andesitic magmas have concluded that H_2O contents >7 wt % are required to produce some andesitic magma compositions [*Anderson*, 1974; *Carmichael*, 2002; *Grove et al.*, 2003]. The high SiO_2 characteristic of subduction magmas may reflect the overall lower equilibration temperatures of hydrous magmas, relative to anhydrous magmas with otherwise similar compositions. It also sug-

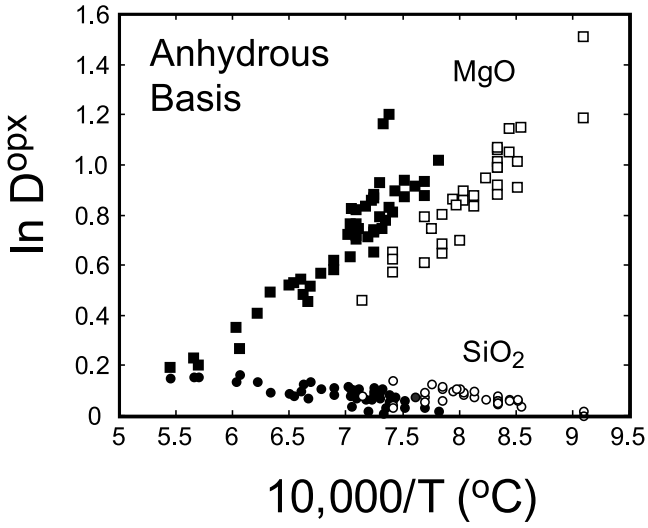

Figure 8. Mineral melt partition coefficients (*D*) for opx in hydrous (open symbols) and anhydrous (solid symbols) for SiO_2 (circles) and MgO (squares). The partition coefficients have been recalculated on an anhydrous basis to remove the effects of dilution by H_2O (see text). The partition coefficient for MgO and SiO_2 diverge at low temperatures, causing a rise in the SiO_2/MgO ratio of the melts.

gests that H_2O contents in subduction related magmas may be far higher than is commonly accepted. In the following section, we present a partitioning based model that predicts melt compositions and corroborates the conclusion that high H_2O contents (>7 wt %) are required to produce many andesites.

6. Melting Model

6.1. Theory

[33] The relatively well behaved element partitioning in high-degree melts can be used to advantage in constructing a predictive melting model [*Weaver and Langmuir*, 1990]. Three equations constrain the composition and weight proportions of phases in equilibrium with each other. The first is mass balance, which states that the mass of an element in each phase must sum to the mass of that element in the bulk composition:

$$\sum_j n_j x_j^i = x_{\text{bulk}}^i \tag{7}$$

where n_j is the weight fraction of phase j, x_j^i is the weight percent of element i in phase j, and x_{bulk}^i is the weight percent of i in the bulk composition. The second constraint is that each phase must be stoichiometric:

$$\sum_i x_j^i = 1 \tag{8}$$

where the summation is over all elements i in phase j.

[34] The third constraint is the equilibrium condition given in equation (1), stating that the partial molar Gibb's free energy of two phases in equilibrium must be equal. Equation (4) recasts this constraint in terms of mineral/melt partition coefficients (D) and gives the temperature dependence. Pressure and compositional terms can be included [e.g., *Ulmer*, 1989] to yield

$$\ln D = a + b/T + cP + d\text{H}_2\text{O}^{\text{melt}} \tag{9}$$

where D is the molar partition coefficient, T is temperature, P is pressure and H_2O^{melt} is the H_2O content of the melt. When the bulk composition of the system is prescribed, equations (7), (8), and (9) leave only two independent variables. For modeling purposes, we have chosen these two variables to be pressure and temperature.

6.2. Parameterization of Partition Coefficients

[35] The core of the model (from here on referred to as HARZ) is the parameterization of the ol/melt and opx/melt D values. The values of the constants in equation (9) have been obtained using linear regression using P, $1/T$, and melt composition as the independent variables (Table 5).

[36] We have sought to find the minimum number of parameters that describe the partitioning. For the majority of oxides, using only the 1/T parameter yields the most significant fit with the smallest errors on the fit parameters. Adding more parameters increases the R^2, but significantly lowers the significance F. SiO_2 partitioning is mostly controlled by H_2O content, but a small temperature or pressure term is also statistically significant. Using both P and T in the regression yielded a low significance, likely because P and T are highly correlated in experimental data sets. The fit using P and H_2O gave slightly better statistics and is the one used in the model. $AlO_{1.5}$ in opx was also found to have a slightly better fit to P and H_2O than to $1/T$.

Table 5. Linear Fit Parameters to Experimental Partitioning Data

	Olivine					
	a[a]	b	c	d	R^2	F[b]
SiO_2	−0.128(7)	–	0.0007(3)	0.505(24)	0.956	854.3
TiO_2	−3.5(16)	2749(2107)	–	–	0.159	7.0
$AlO_{1.5}$	0.19(43)	−3185(580)	–	–	0.628	120.1
$CrO_{1.5}$	−1.13(58)	1336(778)	–	–	0.162	11.8
FeO	−1.17(13)	1685(175)	–	–	0.823	366.1
MnO	−1.30(38)	1698(516)	–	–	0.384	43.0
MgO	−0.81(11)	1841(144)	–	–	0.891	646.3
CaO	−1.30(18)	−482(238)	–	–	0.171	16.3
$NaO_{0.5}$	–	–	–	–	–	–
	Orthopyroxene					
	a[a]	b	c	d	R^2	F
SiO_2	0.016(5)	–	0.0010(2)	0.525(18)	0.978	1725.7
TiO_2	−1.95(56)	1416(757)	–	–	0.164	13.9
$AlO_{1.5}$	−0.494(71)	–	0.003(2)	–	0.044	3.7
$CrO_{1.5}$	−2.16(63)	3723(840)	–	–	0.524	78.0
FeO	−1.42(11)	1757(145)	–	–	0.880	581.2
MnO	−1.23(42)	1606(555)	–	–	0.329	33.3
MgO	1.00(10)	1876(132)	–	–	0.910	793.9
CaO	−0.38(16)	−457(213)	–	–	0.188	18.3
$NaO_{0.5}$	1.77(40)	−4178(551)	–	–	0.802	230.2

[a]Fit parameters to the equation $\ln D^i = a + b/T + c*P + d*H_2O$ for oxide i.
[b]Significance parameter.

[37] The linear fits are of varying quality. Those for SiO_2, MgO, and FeO in both ol and opx are excellent and significant at the 0.005 level or better (Figure 9a). $AlO_{1.5}$ and MnO in ol and $CrO_{1.5}$ and MnO and $NaO_{0.5}$ in opx are intermediate and are significant at the 0.01 level (Figure 9b). TiO_2, $AlO_{1.5}$, and CaO have poor fits in opx and are only significant at the 0.25 level (Figure 9c). TiO_2, $CrO_{1.5}$, and CaO have poor fits in olivine, but as they are minor elements in olivine, this has little effect on the model.

[38] To expand the P-T composition range of the fits, the experimental data from the current study were combined with literature data [*Baker and Stolper*, 1994; *Gaetani and Grove*, 1998; *Hirose and Kawamoto*, 1995; *Kinzler*, 1997; *Walter*, 1998]. The literature data were filtered in the following manner. First, all experiments with Fe-Mg K_D for ol and opx that fall outside of the equilibrium values for alkali-poor compositions (0.33 ± 0.03 and 0.32 ± 0.03, respectively) were removed. Then each experimental partitioning data set was checked for consistency with the current data set and other literature data sets. Clear outliers were removed. Given the simplicity and semiempirical nature of the model, our initial intention was only to include melts saturated with ol and opx. Including the current study, there are only 30 such experiments for which both melt and mineral compositions are available. To increase the data set, ol-opx-cpx-saturated melts were included. Theoretically, the ol-opx-melt partitioning systematics should not be affected by the presence of cpx. On the other hand, the lherzolite-saturated melts generally have higher CaO, Na_2O, and Al_2O_3 contents. Aluminate melt species have been shown to have a significant effect on ol and opx partitioning [*Hirschmann et al.*, 1998a]. The simplicity of the current

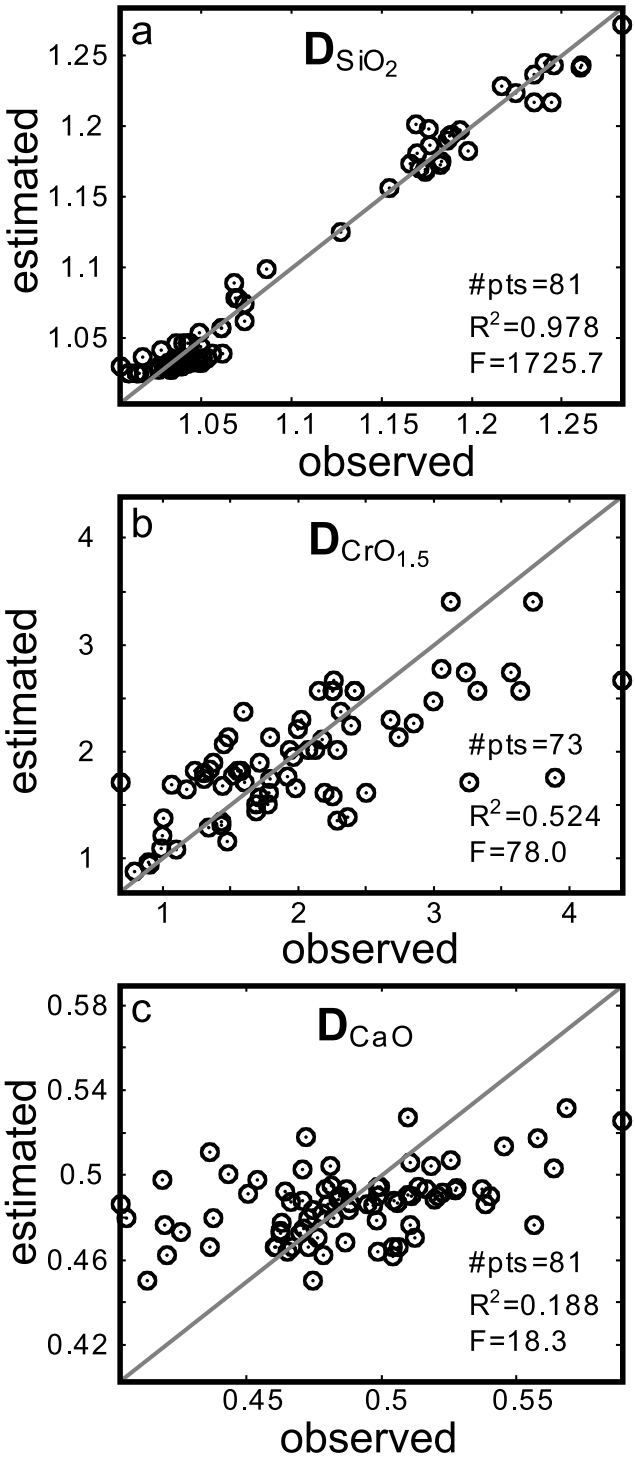

Figure 9. Estimated versus observed opx/melt partition coefficients for (a) SiO_2, (b) $CrO_{1.5}$, and (c) CaO. All phase compositions have been converted to single cation oxides. Points represent measured partition coefficients in experiments, plotted against the estimated partition coefficients using the experimental conditions and products in the predictive equations discussed in the text. For reference, a line with slope of 1 is shown in each plot. The three oxides were selected to display the range of fits from excellent (SiO_2), to good ($CrO_{1.5}$), to poor (CaO). Not all studies report Cr_2O_3 concentrations, so the number of $D_{CrO1.5}$ data points is less than for the major elements (e.g., SiO_2, CaO).

model prevents us from including aluminate melt components in any straightforward manner. Nevertheless, the addition of 50 ol-opx-cpx saturated melts improved the linear regressions of the partitioning data. A total of 81 experiments are included in the data set. The only major experimental study that was not included was that of *Falloon and Danyushevsky* [2000]. Inclusion of this study caused a significant decrease in the quality of the linear regressions. We do not know the reason for this, though we note that the hydrous experiments of Falloon and Danyushevsky were performed in carbon capsules, whereas the other hydrous experiments were performed in metal capsules.

7. Model Results

7.1. Comparison of Predicted Phase Equilibria With Experimental Data

[39] The Newton-Raphson method is used to solve the system of equations (7)–(9). The P, T, and bulk composition of the system are set, as is an initial guess at the melt composition. The P, T, and melt H_2O are used to calculate a set of ol/melt and opx/melt D values. The system of equations is iteratively solved until a minimum level of convergence is reached for all values (0.01% relative, usually requiring less than 20 iterations). A new set of D values is calculated at each step. When the entered pressure-temperature conditions are outside of the stability field of either ol or opx, the model does not converge on positive values for the phase percentages of ol, opx and melt. For a given P and bulk composition, the lowest temperature for which the model converges is taken as the cpx-out point, while the highest temperature where the model converges is taken as the opx-out point.

[40] The first test of the model is how well it reproduces the data included in the database (i.e., the interpolation accuracy of the model). Figure 10 compares the HARZ output with the experiments of *Walter* [1998]. The agreement is excellent. Phase proportions are generally within 0.1 or better. Temperature accuracy can be judged by noting the point where ol and melt have equal fractions. This is predicted within 40°C by the model. The slope of the melt fraction curve (dF/dT = melt productivity) is 0.0016/°C, consistent with previous studies that argue for a low dF/dT after the exhaustion of cpx from the residue [*Hirschmann et al.*, 1999]. Even quite subtle aspects are recovered. From theory [*Asimow et al.*, 1997], it is expected that dF/dT will rise as melting approaches the exhaustion of a phase. This results in a concave up curve of F versus T. This is present in the HARZ predictions and in the Walter data (Figure 10). Note that no phase fraction information is provided to the model, only partitioning data.

[41] Another test of accuracy is to compare the predictions with data not included in the HARZ data set. For this purpose the data of *Falloon and Danyushevsky* [2000] are compared to the model predictions in Figure 11. In that study, the starting composition for the experiments was varied for each run by adding various proportions of boninite melt and harzburgite residue. The points plotted have 20–60% boninite added. For clarity, only the model results for a 50% mixture is shown. The difference in bulk composition contributes minimally to the misfit of the experimental data. The agreement with the experimental

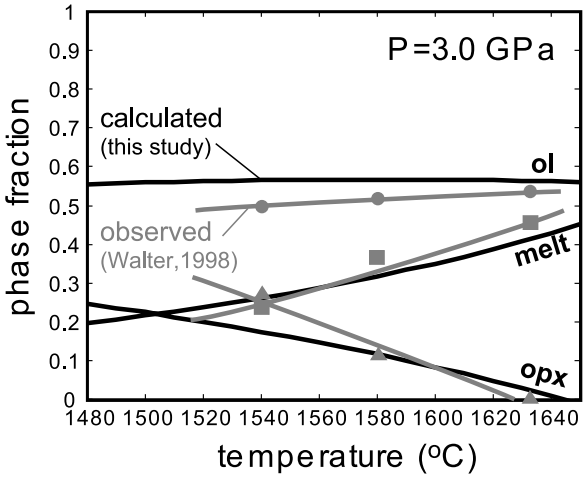

Figure 10. Predicted phase fractions during melting for fertile mantle (anhydrous) compared to published experimental results [*Walter*, 1998]. Pressure is 3.0 GPa. Below 1480°C, the model is does not converge on a real solution, indicating that cpx is a stable phase. The cpx-out point (20% melt) is consistent with previous experiments (19–20% [*Baker and Stolper*, 1994]) and MELTs calculations (18% [*Hirschmann et al.*, 1999]) at 1.0 GPa. The experiments of Walter were part of the data used to calibrate the model, so this plot shows how well the model recovers the input data. Melt fractions are recovered to within ±0.05 and solid fractions to within ±0.1. The melt reaction is also recovered, with opx decreasing rapidly with little change in ol fraction. The opx exhaustion point is reproduced within 20°C. The concave up shape of the melt curve and its slope (0.16% melting/°C is isobaric melt productivity) are consistent with thermodynamic calculations [*Asimow et al.*, 1997; *Hirschmann et al.*, 1999]. Note that no phase fraction data were used to calibrate the model, only partitioning data.

data is excellent, with compositional differences less than 10% relative for the majority of the data points. For the wet experiments, the worst fit compositional parameter is CaO, which is significantly overestimated. This is not surprising as this element is one of the worst fit by the linear models, and should be most affected by aluminate speciation, which is not accounted for in the model. For the dry data, all of the estimates are quite good, likely because there are more anhydrous than hydrous experiments in the model data set, and the experimental difficulties are less, and so the anhydrous data are likely of higher quality.

[42] Another indication of the accuracy of the model is how well it predicts the point of cpx exhaustion. The model of Kinzler and Grove [*Kinzler and Grove*, 1992a, 1993] (from here on referred to as KG93), predicts melt compositions in equilibrium with ol-opx-cpx-spinel. Predicted melt compositions for melting a slightly depleted mantle composition at 1.5 GPa using KG93 are shown in Figure 11. Cpx is exhausted from the residue at a melt fraction of 0.20 at 1378°C. Using the same mantle composition at 1.5 GPa, HARZ does not converge below a melt fraction of 0.15 and a temperature of 1390°C. The compositions of the melts at the cpx exhaustion point predicted by both models are in good agreement. Again, the worst agreement is for CaO, where the discrepancy is over 15% relative. None of the data used for KG93 were used in the current model and the models are significantly different in their approach to predicting melt compositions. The good agreement of such disparate approaches to predicting melt compositions is a good indication of the accuracy of both models. For comparison, pMELTS [*Ghiorso et al.*, 2002] predicts cpx exhaustion at a significantly higher temperature (1440°C), though the melt fraction is similar (0.20). The melt composition predicted by pMELTS is not consistent with either the current model or KG93 with SiO_2 = 44.85 wt % and MgO = 17.75%.

[43] Table 6 compares the accuracy of the current model with existing predictive melting models (HARZ [this study], MELTS [*Ghiorso and Sack*, 1995], pMELTS [*Ghiorso et al.*, 2002], BATCH [*Longhi*, 2002]). The predicted melt compositions, phase fractions and temperatures are compared to 2 anhydrous and 2 hydrous experiments [*Falloon and Danyushevsky*, 2000] that were not part of any of the models' databases. The predictive capability of each model is assessed in two ways. The first compares predicted and observed melt compositions and phase fractions at the same temperature as the experiment, allowing one to evaluate the accuracy of the phase fraction predictions. The second comparison is made by varying temperature until the predicted melt fraction matches the observed melt fraction in the experiment. This allows evaluation of the temperature accuracy of the model. Both methods yield predicted melt compositions. Since mass balance is a fundamental model constraint, errors in melt fraction (F) map directly into melt composition. So comparisons at constant F give a better indication of the ability of the model to predict melt compositions and yield better matches between the predicted and observed melt composition than the constant temperature comparisons. Pressure has not been varied in these comparisons. Because of the covariance of P and T, lowering P at constant T has an effect similar to raising T at constant P (i.e., melt fraction increases).

[44] Overall, HARZ yields the best fit for both wet and dry experiments (Table 6). At constant F, the predictions of HARZ and BATCH for the two anhydrous experiments (T-3569 and T-3520) are remarkably similar and yield the most accurate melt compositions. Errors on the major oxides (SiO_2, Al_2O_3, FeO, MgO and CaO) are all less than 5% relative, and mostly 2% or less. Both HARZ and BATCH predict temperatures that are too high by 30–65°C. The pMELTS model does a better job of predicting temperature with errors of 15–30°C, but the predicted melt compositions have significantly higher errors (up to 14% relative for major oxides SiO2, Al2O3, FeO, MgO, and CaO, with most errors ~5%).

[45] For the hydrous experiments (T-3486 and T-3490), the results are mixed. At 1.5 GPa, the pMELTS program is the most accurate, with errors on the major oxides less than 5% relative and a temperature error of only 10°C. However, at 2.0 GPa, the compositional errors of pMELTS greatly increase (up to 17%), though the temperature accuracy is still excellent (7°C). The pMELTS program is a version of the MELTS program optimized to predict mantle melt compositions near 1 GPa, so its loss of accuracy at higher pressures is not unexpected. At 1.5 GPa, the compositional errors of HARZ are below 10% relative and the temperature

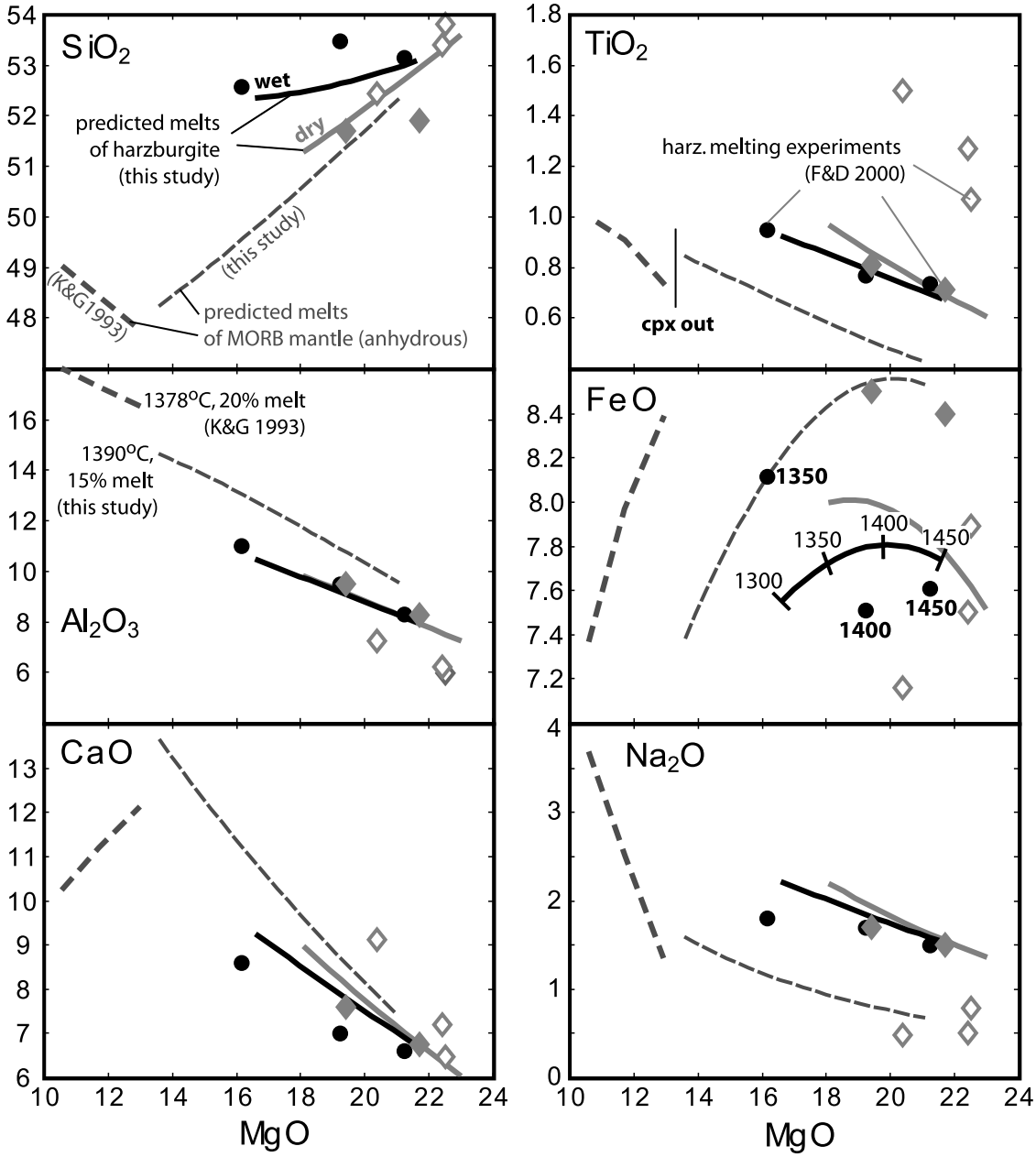

Figure 11. Predicted melt compositions at 1.5 GPa compared to published experiments [*Falloon and Danyushevsky*, 2000] and melting models [*Kinzler and Grove*, 1992a, 1993]. The Falloon and Danyushevsky experiments used various mixtures of a boninite and harzburgite as their starting materials. The solid lines show the predicted melt compositions for 50/50 boninite/harzburgite mixtures with 0% (gray line) and 3% H_2O (black line). The hydrous experiments (black circles) had 35, 45, and 61% (from left to right in the diagram) added boninite, while the dry experiments had 62 and 59 (gray diamonds) and 19, 20, and 17% (open diamonds). The open diamonds fall of the predicted curve for the incompatible elements because of the lower amount of added boninite. These experiments were not used to calibrate the model, and so represent a good test of the model's accuracy. The left sides of the curves represent the point where cpx is exhausted from the residue. The right sides of the curves are where opx is exhausted from the residue. In the FeO plot, the temperatures of the hydrous experiments are shown. The predicted temperatures for the predicted hydrous melting curve are marked in 50°C increments and correspond well to the experimental data. Predicted melts of a slightly depleted (model MORB source), anhydrous composition are also shown. The model of *Kinzler and Grove* [1992a, 1993] is used to model melting up to the cpx-out point (thick dashed line). The model presented in the current text is used to predict melting after cpx-out. Note the good correspondence between the cpx-out points for both models. The composition, melt fraction (given in the Al_2O_3 plot), and temperature are all in good agreement.

Table 6. Comparison of Experiments and Model Predictions

		T-3569[a]	HARZ		pMELTS		MELTS	BATCH	
	Bulk[b]	1480°C	1480°C	1545°C	1480°C	1465°C	1480°C	1480°C	1531°C
P, GPa		1.5	1.5	1.5	1.5	1.5	1.5	1.5	1.5
SiO_2	49.88[c]	51.70	51.00	52.05	50.10	49.70	46.49	51.83	52.38
TiO_2	0.46	0.81	0.95	0.78	0.71	0.79	1.10	0.99	0.79
Al_2O_3	5.65	9.50	10.24	9.01	8.47	9.22	11.88	10.51	9.21
Cr_2O_3	0.13	0.20	0.10	0.13	0.21	0.23	0.10	0.10	0.12
FeO	7.41	8.50	8.43	8.29	8.52	8.72	9.53	8.25	8.21
MnO	0.13	0.15	0.15	0.15	0.10	0.09	0.24	0.16	0.16
MgO	30.38	19.40	17.49	19.85	23.12	21.69	16.92	15.69	19.05
CaO	4.68	7.60	9.13	7.71	6.88	7.46	10.66	9.60	7.75
Na_2O	1.07	1.73	2.26	1.83	1.70	1.89	2.79	2.56	1.92
K_2O	0.11	0.31	0.24	0.19	0.17	0.20	0.29	0.27	0.20
H_2O	0.35	0.70	0.77	0.61	0.56	0.62	0.93	-	-
Melt		0.56[d]	0.45	0.56	0.63	0.56	0.38	0.41	0.56
ol		0.26	0.29	0.29	0.18	0.19	0.18	0.28	0.29
opx		0.18	0.26	0.15	0.20	0.25	0.44	0.31	0.16

		T-3486[a]	HARZ		pMELTS		MELTS
	Bulk	1350°C	1350°C	1410°C	1350°C	1360°C	1350°C
P, GPa		1.5	1.5	1.5	1.5	1.5	1.5
SiO_2	49.07	52.50	50.49	51.04	52.07	52.18	49.23
TiO_2	0.45	0.95	1.07	0.95	0.94	0.91	1.19
Al_2O_3	5.44	11.00	11.40	10.39	11.19	10.81	14.09
Cr_2O_3	0.13	0.19	0.08	0.10	0.29	0.28	0.19
FeO	7.24	8.10	8.11	8.32	7.79	7.84	7.48
MnO	0.13	0.14	0.15	0.15	0.09	0.09	0.26
MgO	30.33	16.10	15.43	17.34	16.09	16.76	12.33
CaO	4.51	8.60	10.35	9.18	8.97	8.68	11.70
Na_2O	1.03	1.80	2.64	2.27	2.30	2.21	3.18
K_2O	0.11	0.46	0.28	0.25	0.25	0.24	0.35
H_2O	1.46	3.00	3.62	3.12	3.18	3.05	4.36
Melt		0.48	0.42	0.48	0.46	0.48	0.34
ol		0.34	0.29	0.29	0.30	0.30	0.26
opx		0.18	0.29	0.23	0.24	0.22	0.40

		T-3520[a]	HARZ		pMELTS		MELTS	BATCH	
	Bulk	1500°C	1500°C	1535°C	1500°C	1530°C	1500°C	1500°C	1551°C
P, GPa		2.0	2.0	2.0	2.0	2.0	2.0	2.00	2.00
SiO_2	50.78	50.20	50.31	50.89	45.68	47.34	43.43	49.93	50.88
TiO_2	0.57	0.87	0.96	0.87	0.99	0.85	1.25	1.09	0.87
Al_2O_3	7.02	9.90	10.39	9.76	10.76	9.59	12.16	10.57	9.68
Cr_2O_3	0.07	0.10	0.05	0.06	0.14	0.11	0.03	0.06	0.06
FeO	8.09	9.50	9.23	9.08	10.79	10.05	11.75	9.55	9.24
MnO	0.13	0.10	0.15	0.15	0.26	0.21	0.34	0.16	0.16
MgO	26.05	18.70	17.16	18.50	19.28	21.36	15.71	14.87	18.26
CaO	5.76	8.60	9.21	8.43	9.15	8.04	11.47	10.59	8.46
Na_2O	1.35	1.70	2.29	2.05	2.61	2.14	3.42	2.87	2.16
K_2O	0.13	0.32	0.23	0.21	0.26	0.21	0.34	0.28	0.21
H_2O	0.00	0.00	0.00	0.00	0.00	0.00	0.00	-	-
melt		0.62	0.55	0.62	0.50	0.62	0.38	0.46	0.46
ol		0.11	0.16	0.16	0.00	0.00	0.00	0.12	0.13
opx		0.27	0.30	0.22	0.50	0.38	0.62	0.42	0.25

		T-3490[a]	HARZ		pMELTS		MELTS
	Bulk	1400°C	1400°C	1405°C	1400°C	1407°C	1400°C
P, GPa		2.0	2.0	2.0	2.0	2.0	2.0
SiO_2	49.71	51.10	50.26	50.32	47.63	47.71	44.60
TiO_2	0.54	0.88	0.94	0.93	0.87	0.85	1.07
Al_2O_3	6.70	11.10	10.66	10.58	10.46	10.21	12.91
Cr_2O_3	0.08	0.11	0.06	0.06	0.14	0.14	0.15
FeO	7.85	8.90	9.05	9.05	9.96	9.91	9.40
MnO	0.12	0.12	0.14	0.14	0.18	0.18	0.25
MgO	26.17	17.20	16.97	17.14	19.54	20.05	12.83
CaO	5.50	8.40	9.34	9.24	8.69	8.48	10.98
Na_2O	1.29	1.70	2.33	2.30	2.31	2.24	3.03
K_2O	0.13	0.39	0.24	0.24	0.24	0.23	0.31
H_2O	1.85	3.10	3.31	3.27	3.24	3.14	4.40
melt		0.59	0.58	0.59	0.57	0.59	0.42
ol		0.16	0.17	0.17	0.05	0.05	0.10
opx		0.24	0.25	0.24	0.38	0.36	0.48

error is 60°C. Of all of the *Falloon and Danyushevsky* [2000] experiments, these are the least well reproduced by HARZ. The accuracy at 2.0 GPa is excellent, with compositional errors less than 5% (except for CaO, which has a 10% error) and a temperature error of only 5°C. It is peculiar that the HARZ model reproduces the *Falloon and Danyushevsky* [2000] experiments over a range of pressure and H_2O contents, except at 1.5 GPa under hydrous conditions. The Falloon and Danyushevsky experiments were not included in the HARZ model because they caused a significant degradation of the linear regressions. It may be that it is the 1.5 GPa hydrous experiments in particular that are not consistent with the other experimental data sets. The BATCH model only predicts anhydrous phase equilibria and so no comparison is possible for hydrous experiments.

[46] The HARZ model generally overpredicts temperatures by up to 60°C, with average errors of 35°C. Typical major oxide errors are 5% relative. TiO_2 concentrations are well reproduced. Cr_2O_3 concentrations are consistently underpredicted (up to 45% relative error). Na_2O is consistently overpredicted, though this may be due to errors in the analysis of the experimental glass, where Na has a tendency to migrate during analysis. The absolute errors on K_2O and MnO are small since they are in such low abundances. Their partitioning behavior is fairly simple (K_2O is incompatible and MnO has $D = 1$), so most of the error is likely to be analytical, either in the experiments that went into the HARZ database or in the *Falloon and Danyushevsky* [2000] experiments. It should also be noted that the Falloon and Danyushevsk*y* experiments were not included in the model data set because they caused a significant decrease in the fits to the partition coefficients, indicating that their results are not consistent with the other experimental studies included in the linear regressions.

[47] In sum, the current model is a significant improvement over existing models for predicting melt compositions of ol-opx saturated melts. For anhydrous experiments, the BATCH model is equally accurate, but it does not predict hydrous phase equilibria. The pMELTS program generally has better temperature accuracy, especially at pressures below 1.5 GPa, but has significantly larger compositional errors under most conditions. The results of the MELTS program are also shown in Table 6. In all cases, they are the least accurate of the four models.

7.2. Effects of H_2O, Bulk Composition, and Pressure

[48] In the current model, only SiO_2 and Al_2O_3 partitioning are direct functions of melt H_2O contents. Mass balance and stoichiometric constraints cause the variations in melt H_2O, SiO_2 and Al_2O_3 contents to affect the concentration of the other elements. The dramatic rise in SiO_2 contents is the most noticable compositional effect of H_2O (Figure 12). With 4 wt % H_2O added to the bulk composition (14 wt % H_2O in the melt), the SiO_2 content of the first melt after the cpx-out point (left end of lines, Figure 12a) rises from 47.7 to 53.8 wt %. H_2O along the 4 wt % bulk H_2O line varies from 14 wt % down to 10 wt % as the melt extent increases (left to right). Because the melting reaction is dominated by opx, the melting curves converge toward its composition as melting extent increases. Part of the convergence of the hydrous and anhydrous curves is also the drop in melt H_2O contents along the curves. The last melt in the ol-opx stability field (right end of the lines) rises only from 51.6 to 53 wt % SiO_2 when 4 wt % H_2O is added (10 wt % H_2O in melt).

[49] It is well known that H_2O lowers the melting temperatures of silicates. In the current model, there is no explicit relationship between H_2O and temperature. Rather, the addition of H_2O lowers the concentrations of all other elements in the melt by dilution, while the composition of the solids is not directly affected (H_2O is assumed to be totally incompatible). This increases the apparent D values for all elements. Since all of the D values (except $NaO_{0.5}$) are inversely related to temperature, the higher D values are translated into lower equilibration temperatures. In practice, the temperature is prescribed, so the model responds to added H_2O by increasing melting extents.

[50] For most elements, the effect of H_2O to decrease equilibration temperatures and thereby increase partition coefficients, causes element concentrations in the melt to decrease with added H_2O. The effect is greatest for MgO, which can be seen in the shift of the curves in Figure 12 to lower melt MgO contents. Concentrations of the remaining elements decrease to a lesser extent, and large amounts of H_2O (>3 wt %) are required to produce a noticable change in their concentrations.

7.3. Effect of Source Depletion

[51] The effect of melting a depleted source is also shown in Figure 12. The bulk composition used is a 50/50 mix of a fertile mantle composition (MM3 [*Walter*, 1998]) and a harzburgite (2PKI-38 [*Falloon and Danyushevsky*, 2000]) and represents a moderately depleted mantle source. Because the melting reaction is so dominated by opx, one can think of the melting curves as mixing curves between the low SiO_2, low MgO melt at the cpx-out point and the composition of the opx entering the melt (plus or minus a small amount of olivine). The more depleted the source, the less of the low SiO_2, low MgO melt is present, allowing the melting curves to shift toward the composition of opx. The increase in compatible element concentrations lowers their partition coefficients, which is reflected in higher equilibration temperatures (Figure 12).

7.4. Effect of Pressure

[52] As with the effect of H_2O, only SiO_2 and Al_2O_3 partitioning are directly affected by pressure in our model. Pressure dramatically lowers SiO_2 contents, and thereby increases the concentrations of all other elements in the melt (Figure 13). The result is that the effect of pressure is almost exactly opposite the effect of H_2O.

Notes to Table 6.

[a] Experiment of *Falloon and Danyushevsky* [2000].

[b] Bulk composition of the experiment and used in the predictive models.

[c] Weight percent.

[d] Weight fraction of phase.

This is consistent with previous observations of the competing effects of H_2O and pressure on phase boundaries [*Gaetani and Grove*, 1998].

[53] The effect of H_2O on melt composition is also pressure dependent. At low pressures (1–2 GPa), the anhydrous and 1.5 wt % H_2O melting curves overlap for all elements except SiO_2 and MgO. At 6.0 GPa, the Al_2O_3 concentrations of the hydrous melts near the cpx-out boundary (left side of curves) are distinctly higher in the hydrous melts while FeO contents are lower. At higher degrees of melting, the dry and wet melt compositions converge as they approach the composition of opx, and the effect of pressure is less pronounced. The effect of H_2O on SiO_2 contents, on the other hand, varies little with pressure (Figure 13).

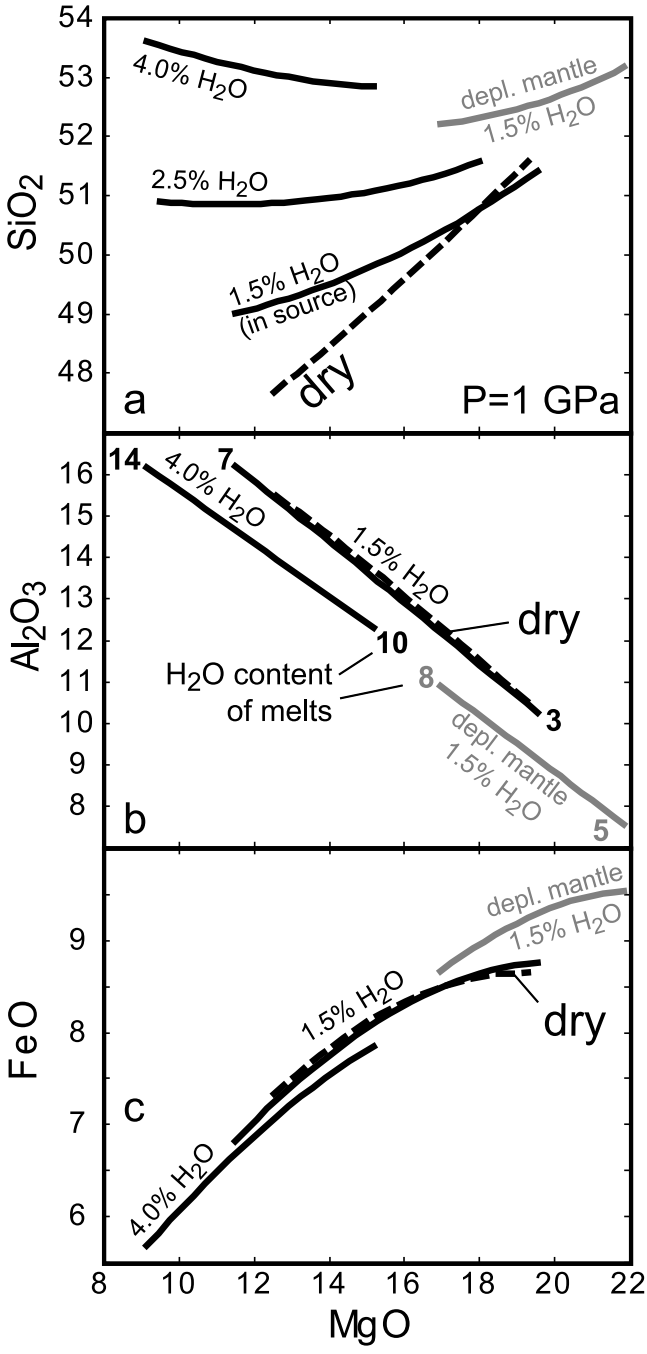

Figure 12. (a) SiO_2, (b) Al_2O_3, and (c) FeO contents of predicted melts versus MgO content displaying the effect of H_2O and source depletion at 1 GPa. Black lines show effect of increasing bulk H_2O. Lines are labeled with the bulk H_2O content (in weigh percent). Dashed line is for anhydrous model. As melting proceeds, melt H_2O contents decrease because of dilution. Melt H_2O contents at the beginning and ending of melting are labeled in the Al_2O_3 plot. For clarity, the 2.5% H_2O curve is not shown in Figures 12b and 12c. H_2O increases SiO_2 and lowers Al_2O_3 and FeO, at a given MgO content. The cpx and opx exhaustion points (left and right sides of curves) shift to lower MgO values. The effect of water decreases as melting progresses partly due to the decreasing melt H_2O content and partly due to the fact that ol becomes the only remaining solid. Melting a more depleted source shortens the melting curves and shifts them to higher MgO and FeO concentrations and lower Al_2O_3 concentrations.

7.5. Empirical Versus Thermodynamic Modeling

[54] Fully thermodynamic models such as MELTS have the ambitious goal of relating phase compositions to thermodynamic state functions over a wide range of compositions and stable phases [*Ghiorso*, 1991; *Ghiorso and Sack*, 1995]. The current semiempirical model has the more modest goal of predicting melt compositions in equilibrium with ol and opx. By limiting the scope of the model, substantial accuracy has been achieved with a relatively simple model, though at the sacrifice of insight into the underlying thermodynamic controls. The limited scope of the current model allows it to be modified readily, and in particular, the database of experiments on which it is based can be changed. This is a useful feature, as new experimental melting data (especially hydrous experiments) are steadily being produced.

8. Conclusions

[55] A partitioning-based numerical model has been constructed that predicts the composition of melts in equilibrium with ol and opx under both hydrous and anhydrous conditions. The composition of the solid phases and the mass proportions of all phases are also predicted. The model inputs are pressure, temperature and the bulk composition of the system. The model is more accurate than any extant model, with typical compositional errors of 1–5% relative for the major oxides. Typical errors on temperature are 30–40°C.

[56] The experimental data indicate that at mantle temperatures, H_2O predominantly dissolves into silicate melts as dissociated OH^-. For a given bulk composition, the effect of H_2O on SiO_2 activity coefficients is primarily thermal, and suggest a two-lattice model for the mixing of melt species [*Drake*, 1976]. The experimental data also indicate that hydrous magmas are not intrinsically higher in SiO_2 than anhydrous melts. We propose that the high SiO_2 character of subduction-related magmas is predominantly a temperature effect and that mafic, high-SiO_2 (>54 wt %)

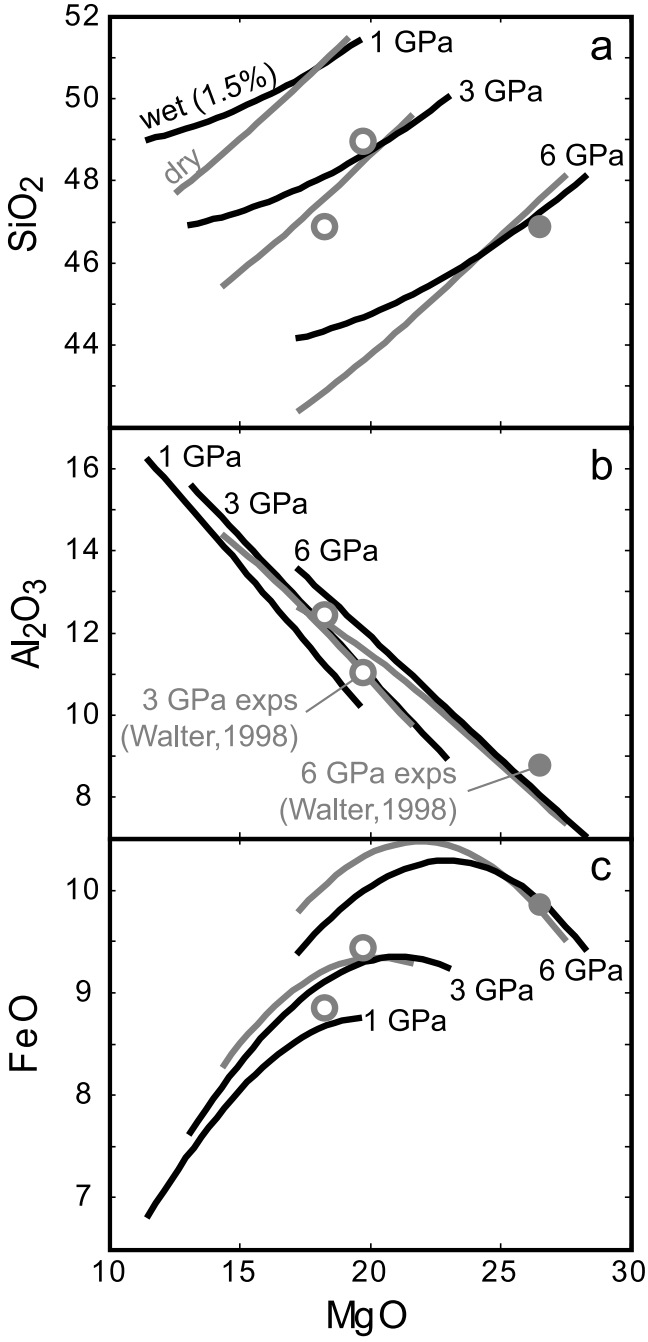

Figure 13. (a) SiO_2, (b) Al_2O_3 and (c) FeO contents of predicted melts versus MgO content displaying the effect of pressure on wet (black lines, 1.5% H_2O) and dry (gray lines) melting of fertile mantle composition. Experiments of *Walter* [1998] at 3 GPa (open symbols) and 6 GPa (gray symbol) are shown for comparison. Increasing pressure lowers SiO_2 and Al_2O_3 and raises FeO and MgO contents. Note that the effect of H_2O on SiO_2 contents changes little with increasing pressure. At 1 GPa for Al_2O_3 and FeO, the wet and dry melting curves are essentially coincidental and only the wet curve is shown.

andesites require H_2O contents >7 wt % to lower melting temperatures to the appropriate levels.

[57] **Acknowledgments.** We would like to thank Marc Hirschmann and Mark Ghiorso for help with the MELTS and pMELTS calculations, and John Longhi for use of and help with the BATCH program. Conversations with Glenn Gaetani, Othmar Muentener and Peter Kelemen have greatly benefited this research. Analysis of the run products by EMPA was made possible by the excellent guidance and advice of Neel Chatterjee (MIT Microprobe Facility). This research was supported by NSF grants EAR-9526702 and EAR-9706214.

References

Anderson, A. T., Jr. (1974), Evidence for a picritic, volatile-rich magma beneath Mt. Shasta, California, *J. Petrol.*, *15*(2), 243–267.

Armstrong, J. T. (1995), CITZAF—A package of correction programs for the quantitative electron microbeam X-ray-analysis of thick polished materials, thin-films, and particles, *Microbeam Anal.*, *4*(3), 177–200.

Asahara, Y., and E. Ohtani (2001), Melting relations of the hydrous primitive mantle in the CMAS- H_2O system at high pressures and temperatures, and implications for generation of komatiites, *Phys. Earth Planet. Inter.*, *125*(1–4), 31–44.

Asimow, P. D., and M. S. Ghiorso (1998), Algorithmic modifications extending MELTS to calculate subsolidus phase relations, *Am. Mineral.*, *83*(9–10), 1127–1132.

Asimow, P. D., M. M. Hirschmann, and E. M. Stolper (1997), An analysis of variations in isentropic melt productivity, *Philos. Trans. R. Soc. London, Ser. A*, *355*(1723), 255–281.

Baker, M. B., and E. M. Stolper (1994), Determining the composition of high-pressure mantle melts using diamond aggregates, *Geochim. Cosmochim. Acta*, *58*(13), 2811–2827.

Baker, M. B., T. L. Grove, and R. Price (1994), Primitive basalts and andesites from the Mt Shasta region, N California—Products of varying melt fraction and water- content, *Contrib. Mineral. Petrol.*, *118*(2), 111–129.

Baker, M. B., M. M. Hirschmann, M. S. Ghiorso, and E. M. Stolper (1995), Compositions of near-solidus peridotite melts from experiments and thermodynamic calculations, *Nature*, *375*(6529), 308–311.

Borisov, A., and H. Palme (2000), Solubilities of noble metals in Fe-containing silicate melts as derived from experiments in Fe-free systems, *Am. Mineral.*, *85*(11–12), 1665–1673.

Bottinga, Y. (1972), Thermal aspects of seafloor spreading, *Eos Trans. AGU*, *53*(4), 537.

Burnham, C. W. (1975), Water and magmas; a mixing model, *Geochim. Cosmochim. Acta*, *39*(8), 1077–1084.

Carmichael, I. S. E. (2002), The andesite aqueduct: Perspectives on the evolution of intermediate magmatism in west-central (105–99°W) Mexico, *Contrib. Mineral. Petrol.*, *143*(6), 641–663.

Clague, D. A., W. S. Weber, and J. E. Dixon (1991), Picritic glasses from Hawaii, *Nature*, *353*(6344), 553–556.

Dick, H. J. B., R. L. Fisher, and W. B. Bryan (1984), Mineralogic variability of the uppermost mantle along mid-ocean ridges, *Earth Planet. Sci. Lett.*, *69*(1), 88–106.

Dingwell, D. B., and S. L. Webb (1990), Relaxation in silicate melts, *Eur. J. Mineral.*, *2*(4), 427–449.

Drake, M. J. (1976), Plagioclase-melt equilibria, *Geochim. Cosmochim. Acta*, *40*(4), 457–465.

Falloon, T. J., and L. V. Danyushevsky (2000), Melting of refractory mantle at 1.5, 2 and 2.5 GPa under, anhydrous and H_2O-undersaturated conditions: Implications for the petrogenesis of high-Ca boninites and the influence of subduction components on mantle melting, *J. Petrol.*, *41*(2), 257–283.

Falloon, T. J., and D. H. Green (1987), Anhydrous partial melting of MORB pyrolite and other peridotite compositions at 10 kbar—Implications for the origin of primitive MORB glasses, *Mineral. Petrol.*, *37*(3–4), 181–219.

Falloon, T. J., D. H. Green, C. J. Hatton, and K. L. Harris (1988), Anhydrous partial melting of a fertile and depleted peridotite from 2-Kb to 30-Kb and application to basalt petrogenesis, *J. Petrol.*, *29*(6), 1257–1282.

Gaetani, G. A., and T. L. Grove (1998), The influence of water on melting of mantle peridotite, *Contrib. Mineral. Petrol.*, *131*(4), 323–346.

Ghiorso, M. S. (1991), Thermodynamics of minerals and melts, *Rev. Geophys.*, *29*, 446–456.

Ghiorso, M. S., and R. O. Sack (1995), Chemical mass-transfer in magmatic processes. 4. A revised and internally consistent thermodynamic model for the interpolation and extrapolation of liquid-solid equilibria in magmatic systems at elevated-temperatures and pressures, *Contrib. Mineral. Petrol.*, *119*(2–3), 197–212.

Ghiorso, M. S., M. M. Hirschmann, P. W. Reiners, and V. C. Kress III (2002), The pMELTS: A revision of MELTS for improved calculation of phase relations and major element partitioning related to partial melting of the mantle to 3 GPa, *Geochem. Geophys. Geosyst.*, *3*(5), 1030, doi:10.1029/2001GC000217.

Gill, J. B. (1981), *Orogenic Andesites and Plate Tectonics*, 401 pp., Springer-Verlag, New York.

Green, D. H. (1976), Experimental testing of "equilibrium" partial melting of peridotite under water-saturated, high-pressure conditions, *Can. Mineral.*, *14*(3), 255–268.

Green, D. H., T. Falloon, S. M. Eggins, and G. M. Yaxley (2001), Primary magmas and mantle temperatures, Experimental mineralogy, petrology and geochemistry, *Eur. J. Mineral.*, *13*(3), 437–451.

Grove, T. L. (1981), Use of Fe-Pt alloys to eliminate the iron loss problem in 1 atmosphere gas mixing experiments; theoretical and practical considerations, *Contrib. Mineral. Petrol.*, *78*(3), 298–304.

Grove, T. L., L. T. Elkins-Tanton, S. W. Parman, N. Chatterjee, O. Muentener, and G. A. Gaetani (2003), Fractional crystallization and mantle melting controls on calc-alkaline differentiation trends, *Contrib. Mineral. Petrol.*, *145*, 515–533.

Hays, J. F. (1967), Lime-alumina-silica, *Year Book Carnegie Inst. Washington*, *65*, 234–239.

Hesse, M., and T. Grove (2002), Absarokites from the western Mexican volcanic zone: Constraints on mantle wedge conditions, *Geochim. Cosmochim. Acta*, *66*(15A), A325–A325.

Hirose, K., and T. Kawamoto (1995), Hydrous partial melting of lherzolite at 1 GPa—The effect of H_2O on the genesis of basaltic magmas, *Earth Planet. Sci. Lett.*, *133*(3–4), 463–473.

Hirose, K., and I. Kushiro (1993), Partial melting of dry peridotites at high pressures: Determination of compositions of melts segregated from peridotite using aggregates of diamond, *Earth Planet. Sci. Lett.*, *114*(4), 477–489.

Hirschmann, M. M., M. B. Baker, and E. M. Stolper (1998a), The effect of alkalis on the silica content of mantle-derived melts, *Geochim. Cosmochim. Acta*, *62*(5), 883–902.

Hirschmann, M. M., M. S. Ghiorso, L. E. Wasylenki, P. D. Asimow, and E. M. Stolper (1998b), Calculation of peridotite partial melting from thermodynamic models of minerals and melts. I. Review of methods and comparison with experiments, *J. Petrol.*, *39*(6), 1091–1115.

Hirschmann, M. M., P. D. Asimow, M. S. Ghiorso, and E. M. Stolper (1999), Calculation of peridotite partial melting from thermodynamic models of minerals and melts. III. Controls on isobaric melt production and the effect of water on melt production, *J. Petrol.*, *40*(5), 831–851.

Ihinger, P. D., Y. X. Zhang, and E. M. Stolper (1999), The speciation of dissolved water in rhyolitic melt, *Geochim. Cosmochim. Acta*, *63*(21), 3567–3578.

Ito, K., and G. C. Kennedy (1967), Melting and phase relations in a natural peridotite to 40 kilobars, *Am. J. Sci.*, *265*(6), 519–538.

Jaques, A. L., and D. H. Green (1980), Anhydrous melting of peridotite at 0–15 Kb pressure and the genesis of tholeiitic basalts, *Contrib. Mineral. Petrol.*, *73*(3), 287–310.

Kawamoto, T., and J. R. Holloway (1997), Melting temperature and partial melt chemistry of H_2O-saturated mantle peridotite to 11 gigapascals, *Science*, *276*(5310), 240–243.

Kawamoto, T., R. L. Hervig, and J. R. Holloway (1996), Experimental evidence for a hydrous transition zone in the early Earth's mantle, *Earth Planet. Sci. Lett.*, *142*(3–4), 587–592.

Kinzler, R. J. (1997), Melting of mantle peridotite at pressures approaching the spinel to garnet transition: Application to mid-ocean ridge basalt petrogenesis, *J. Geophys. Res.*, *102*(B1), 853–874.

Kinzler, R. J., and T. L. Grove (1992a), Primary magmas of mid-ocean ridge basalts: 1. Experiments and methods, *J. Geophys. Res.*, *97*(B5), 6885–6906.

Kinzler, R. J., and T. L. Grove (1992b), Primary magmas of mid-ocean ridge basalts: 2. Applications, *J. Geophys. Res.*, *97*(B5), 6907–6926.

Kinzler, R. J., and T. L. Grove (1993), Corrections and further discussion of the primary magmas of mid-ocean ridge basalts, 1 and 2, *J. Geophys. Res.*, *98*(B12), 22,339–22,347.

Kushiro, I. (1968), Compositions of magmas formed by partial zone melting of the Earth's upper mantle, *J. Geophys. Res.*, *73*(2), 619–634.

Kushiro, I. (1972), Effect of water on the composition of magmas formed at high pressures, *J. Petrol.*, *13*(2), 311–334.

Longhi, J. (2002), Some phase equilibrium systematics of lherzolite melting: I, *Geochem. Geophys. Geosyst.*, *3*(3), 1020, doi:10.1029/2001GC000204.

Mckenzie, D., and M. J. Bickle (1988), The volume and composition of melt generated by extension of the lithosphere, *J. Petrol.*, *29*(3), 625–679.

Mysen, B. O., and A. L. Boettcher (1975), Melting of a hydrous mantle I, Phase relations of natural peridotite at high pressures and temperatures with controlled activities of water, carbon dioxide, and hydrogen, *J. Petrol.*, *16*(3), 520–548.

Niu, Y. L., and R. Batiza (1991), An empirical method for calculating melt compositions produced beneath mid-ocean ridges: Application for axis and off-axis (seamounts) melting, *J. Geophys. Res.*, *96*(B13), 21,753–21,777.

Parman, S. W., J. C. Dann, T. L. Grove, and M. J. de Wit (1997), Emplacement conditions of komatiite magmas from the 3.49 Ga Komati Formation, Barberton Greenstone Belt, South Africa, *Earth Planet. Sci. Lett.*, *150*(3–4), 303–323.

Presnall, D. C., J. R Dixon, T. H. O'Donnell, and S. A. Dixon (1979), Generation of mid-ocean ridge tholeiites, *J. Petrol.*, *20*(1), 3–35.

Robinson, J. A. C., B. J. Wood, and J. D. Blundy (1998), The beginning of melting of fertile and depleted peridotite at 1.5 GPa, *Earth Planet. Sci. Lett.*, *155*(1–2), 97–111.

Ryerson, F. J. (1985), Oxide solution mechanisms in silicate melts: Systematic variations in the activity coefficient of SiO_2, *Geochim. Cosmochim. Acta*, *49*(3), 637–649.

Shen, A., and H. Keppler (1995), Infrared spectroscopy of hydrous silicate melts to 1000 degrees C and 10 kbar: Direct observation of H_2O speciation in a diamond-anvil cell, *Am. Mineral.*, *80*(11–12), 1335–1338.

Stern, R. J., and S. H. Bloomer (1992), Subduction zone infancy: Examples from the Eocene Izu-Bonin-Mariana and Jurassic California arcs, *Geol. Soc. Am. Bull.*, *104*(12), 1621–1636.

Stolper, E. (1980), A phase diagram for mid-ocean ridge basalts: Preliminary results and implications for petrogenesis, *Contrib. Mineral. Petrol.*, *74*(1), 13–27.

Stolper, E. (1982a), The speciation of water in silicate melts, *Geochim. Cosmochim. Acta*, *46*(12), 2609–2620.

Stolper, E. (1982b), Water in silicate glasses: An infrared spectroscopic study, *Contrib. Mineral. Petrol.*, *81*(1), 1–17.

Takahashi, E., T. Shimazaki, Y. Tsuzaki, and H. Yoshida (1993), Melting study of a peridotite KLB-1 to 6.5 GPa, and the origin of basaltic magmas, *Philos. Trans. R. Soc. London, Ser. A*, *342*(1663), 105–120.

Ulmer, P. (1989), The dependence of the Fe-2+-Mg cation partitioning between olivine and basaltic liquid on pressure, temperature and composition: An experimental study to 30 Kbars, *Contrib. Mineral. Petrol.*, *101*(3), 261–273.

Wagner, T. P., and T. L. Grove (1998), Melt/harzburgite reaction in the petrogenesis of tholeiitic magma from Kilauea Volcano, Hawaii, *Contrib. Mineral. Petrol.*, *131*(1), 1–12.

Walter, M. J. (1998), Melting of garnet peridotite and the origin of komatiite and depleted lithosphere, *J. Petrol.*, *39*(1), 29–60.

Weaver, J. S., and C. H. Langmuir (1990), Calculation of phase equilibrium in mineral melt systems, *Comput. Geosci.*, *16*(1), 1–19.

Withers, A. C., Y. X. Zhang, and H. Behrens (1999), Reconciliation of experimental results on H_2O speciation in rhyolitic glass using in-situ and quenching techniques, *Earth Planet. Sci. Lett.*, *173*(3), 343–349.

T. L. Grove and S. W. Parman, Department of Earth, Atmosphere, and Planetary Sciences, 54-1224, Massachusetts Institute of Technology, Cambridge, MA 02140, USA. (parman@mit.edu)